

An implicit shock tracking method for simulation of shock-dominated flows over complex domains using mesh-based parametrizations

Alexander M. Pérez Reyes^{a,1}, Matthew J. Zahr^{a,2,*}

^a*Department of Aerospace and Mechanical Engineering, University of Notre Dame, Notre Dame, IN 46556, United States*

Abstract

A mesh-based parametrization is a parametrization of a geometric object that is defined solely from a mesh of the object, e.g., without an analytical expression or computer-aided design (CAD) representation of the object. In this work, we propose a mesh-based parametrization of an arbitrary d' -dimensional object embedded in a d -dimensional space using tools from high-order finite elements. Using mesh-based parametrizations, we construct a boundary-preserving parametrization of the nodal coordinates of a computational mesh that ensures all nodes remain on all their original boundaries. These boundary-preserving parametrizations allow the nodes of the mesh to move only in ways that will not change the computational domain. They also ensure nodes will not move between boundaries, which would cause issues assigning boundary conditions for partial differential equation simulations and lead to inaccurate geometry representations for non-smooth boundary transitions. Finally, we integrate boundary-preserving, mesh-based parametrizations into high-order implicit shock tracking, an optimization-based discontinuous Galerkin method that moves nodes to align mesh faces with non-smooth flow features to represent them perfectly with inter-element jumps, leaving the intra-element polynomial basis to represent smooth regions of the flow with high-order accuracy. Mesh-based parametrizations enable implicit shock tracking simulations of shock-dominated flows over geometries without simple analytical parametrizations. Several demonstrations of mesh-based parametrizations are provided to: (1) give concrete examples of the formulation, (2) show that accurate parametrizations can be obtained despite the surrogate surfaces only being C^0 , (3) show they integrate seamlessly with implicit shock tracking and can be used to parametrize surfaces without explicit expressions (e.g., RAE2822 airfoil), and (4) effectively parametrize complex geometries and prevent nodes from moving off their original boundaries.

Keywords: Surface parametrization, mesh-based parametrization, shock fitting, high-order methods, discontinuous Galerkin, shock-dominated flows

1. Introduction

High-order discontinuous Galerkin (DG) methods [5, 13] offer unique advantages for fluid flow simulations such as high accuracy per degree of freedom, low dissipation, and the ability to handle complex geometries. However, high-speed flows remain challenging because spurious oscillations arise near shock waves and contact discontinuities that impact the accuracy of the flow approximation and lead to solver failure. These issues are exacerbated as the Mach and Reynolds number of the flow increase or the complexity and bluntness of the vehicle increase. Robust and accurate methods to stabilize DG discretizations for realistic shock-dominated flows are needed to make them competitive for real-world aerospace applications [37].

Shock-capturing methods, including limiting [35], reconstruction [12, 21, 15], and artificial viscosity [28, 2], are the most popular stabilization methods. They smear non-smooth features sufficiently so they are well-represented on the grid and, as such, they can handle complex shock structures. However, they are first-order accurate, at best, near shocks and contacts, which must be offset with extremely fine meshes in these regions. On the other hand, shock tracking methods move the grid to align mesh faces with non-smooth

*Corresponding author

Email addresses: aperez23@nd.edu (Alexander M. Pérez Reyes), mzahr@nd.edu (Matthew J. Zahr)

¹Graduate Student, Department of Aerospace and Mechanical Engineering, University of Notre Dame

²Assistant Professor, Department of Aerospace and Mechanical Engineering, University of Notre Dame

features [23, 31], which do not require stabilization because the non-smooth features are represented perfectly with inter-elements jumps in the basis. As such, shock tracking methods are much more accurate than shock capturing methods; however, they are usually limited to simple problems with basic shock structures [32, 33, 36] and require dimension-dependent algorithms [11, 10, 3].

A new class of high-order methods, *implicit shock tracking*, has recently emerged, including the Moving Discontinuous Galerkin Method with Interface Condition Enforcement (MDG-ICE) [6, 16, 17] and High-Order implicit Shock Tracking (HOIST) method [39, 41, 14]. Like traditional shock tracking, these methods seek to align mesh faces with solution features; however, the grid is implicitly defined as the solution of an optimization problem. As such, they transform a shock-agnostic mesh into one aligned with all non-smooth flow features, and simultaneously compute a high-order accurate flow solution on the aligned grid. This key innovation has enabled the benefits of shock tracking to be realized for flows with complex shock structure (e.g., shock intersections, curved shocks, shock formation) [6, 8, 7, 41, 14, 24].

An integral component of implicit shock tracking methods is an approach to ensure the boundaries of the domain are unchanged as nodes move to track the shocks. This condition will be satisfied if the nodes on each domain boundary are fixed to their original position; however, this stringent requirement will prevent the grid from aligning with shocks that impinge on a domain boundary (e.g., transonic, inviscid flows) or lead to highly distorted grids for problems with shocks near boundaries (e.g., hypersonic flows or shock-boundary layer interaction). A more realistic approach uses explicit parametrizations—a mapping from generalized coordinates in the intrinsic dimension of a geometric object to the object itself in the embedding space—of the object on which each node lies (e.g., a boundary or intersection of boundaries) to slide nodes along their original boundaries [41, 14]. That is, for each node i in the computational mesh, we introduce a generalized coordinate \mathbf{y}_i and a mapping ϕ_i from the parameter domain to the physical nodal coordinate $\mathbf{x}_i = \phi_i(\mathbf{y}_i)$ that is constructed to ensure \mathbf{x}_i remains on its original boundaries for any \mathbf{y}_i . Then, instead of directly optimizing for \mathbf{x}_i —which would need to be constrained to lie on its original boundaries—we optimize for \mathbf{y}_i and reconstruct the nodal coordinate as $\phi_i(\mathbf{y}_i)$, which will, by construction, lie on the same boundaries as node i before mesh motion. These boundary-preserving parametrizations have been effectively integrated into implicit shock tracking methods; however, they have only proven useful for relatively simple domains, i.e., domains with planar boundaries or boundaries that can be explicitly parametrized with analytical functions [41, 14, 8]. This work introduces a general procedure to construct boundary-preserving parametrizations directly from a conforming, high-order mesh of the domain, which allows implicit shock tracking to be applied to a new class of problems with complex geometries.

In this work, we parametrize d' -dimensional objects embedded in a d -dimensional space by constructing a surrogate object from a high-order mesh and use finite element tools to parametrize the surrogate. We refer to such parametrizations as *mesh-based parametrizations* because they are defined exclusively from a high-order mesh of an object. Because mesh-based parametrizations are defined elementwise, efficient implementation relies on a fast, reliable approach to find the elements in a high-order mesh in which an arbitrary point in the parameter space lies. We introduce an efficient search algorithm that associates a collection of points with elements of the mesh and uses KD trees to efficiently find the points (and therefore elements) closest to an arbitrary evaluation point. Next, mesh-based parametrizations are used to parametrize the nodal coordinates of a computational mesh in such a way that nodes slide along all their original boundaries. This ensures the shape of the boundaries will not change and a computational face will never straddle two boundaries, which would lead to difficulties assigning boundary conditions and poor geometry representation if the transition between boundaries is not smooth. Finally, these boundary-preserving mesh-based parametrizations are integrated into an implicit shock tracking method so these methods can be applied to a wider class of shock-dominated flow problems, e.g., flows over geometries that do not admit simple explicit parametrizations. The novelty of this work lies in: (1) the formalization of mesh-based parametrizations, (2) an efficient search algorithm to locate elements containing an arbitrary point in a high-order mesh, (3) the use of mesh-based parametrizations to construct boundary-preserving parametrizations of the nodal coordinates of a computational mesh, and (4) the integration of boundary-preserving mesh-based parametrization into implicit shock tracking and demonstration of the new capabilities.

Another common approach to parametrize objects, particularly in the mesh generation community, uses computer-aided design (CAD) representation of the object [38, 34, 9]. Despite being the most general approach to parametrize objects, it comes with a number of limitations in the context of implicit shock tracking. First, CAD geometries are often not sufficiently clean to parametrize objects such that mesh nodes

can seamlessly transition between different NURBS patches, for example. Second, there are many CAD file formats, most of which support a huge number of geometric objects, which makes working with them cumbersome. Finally, derivatives of the parametrization, required by implicit shock tracking solvers, are usually not available through CAD systems. Explicit parametrizations can be avoided by combining an implicit representation of the surface, i.e., a level set function, with a variational penalty function to force nodes onto surfaces [18, 1, 22]. While these methods effectively place faces (and therefore nodes) of a mesh onto the implicitly defined surface, they cannot handle non-smooth features or transitions, which exist in all relevant geometries, particularly aerospace vehicles (e.g., Section 4.3-4.4).

The remainder of the paper is organized as follows. Section 2 introduces the concept of mesh-based parametrizations of arbitrary geometric objects, uses them to construct a boundary-preserving parametrization of the nodes of a computational mesh, and introduces an efficient search algorithm to locate the elements of a high-order mesh in which an arbitrary point lies, a central ingredient for the implementation of mesh-based parametrizations. Section 3 integrates mesh-based parametrizations into the High-Order Implicit Shock Tracking method. Section 4.1 provides two concrete examples of the mesh-based parametrization ingredients and shows the error between the surrogate and true surfaces rapidly decreases under mesh refinement. Sections 4.2-4.3 show mesh-based parametrizations integrate cleanly with implicit shock tracking, where solver convergence and highly accurate, grid-aligned solutions are obtained. Section 4.4 demonstrates mesh-based parametrizations for a complex geometry (sliced cone flap) with multiple surfaces and non-smooth transitions between them.

2. Mesh-based parametrization

In this section we introduce the concept of a mesh-based parametrization, a parametric representation of geometric objects defined solely from a high-order (geometry) mesh of the objects, assuming a complete mathematical or CAD description is unavailable (Section 2.1). These parametrizations are used to construct a mesh-based parametrization of an entire computational mesh (Section 2.2) that guarantees nodes remain on their original surfaces regardless of perturbations to them *in the parameter domain*. We close this section with an efficient strategy to identify the element(s) of a high-order (curved) mesh in which an arbitrary point lies (Section 2.3), which is integral to efficient implementation of mesh-based parametrization.

2.1. Mesh-based parametrization of embedded geometric object

Consider a d' -dimensional geometric object embedded in d dimensions, $\mathcal{S} \subset \mathbb{R}^d$ ($d' < d$). We are mainly interested in curves ($d' = 1$) and surfaces ($d' = d - 1$); however, the development in this section is general. Let $\hat{\mathcal{S}}_{h',q'} \in 2^{\mathbb{R}^d}$ be a high-order mesh of \mathcal{S} with mesh size parameter (longest edge) $h' \in \mathbb{R}_{\geq 0}$ and polynomial degree q' , where 2^S is the power set (set of all subsets) of S . That is, $\hat{\mathcal{S}}_{h',q'}$ is a discretization of \mathcal{S} into non-overlapping, potentially curved, d' -dimensional elements (embedded in \mathbb{R}^d). Because the mesh $\hat{\mathcal{S}}_{h',q'}$ will not, in general, perfectly represent the original object \mathcal{S} , we define the surrogate object $\mathcal{S}_{h',q'} \subset \mathbb{R}^d$ as

$$\mathcal{S}_{h',q'} := \bigcup_{K \in \hat{\mathcal{S}}_{h',q'}} K. \quad (1)$$

We assume the mesh $\hat{\mathcal{S}}_{h',q'}$ is built from conforming Lagrangian finite elements to ensure the surrogate $\mathcal{S}_{h',q'}$ is globally C^0 . The remainder of this section will construct a parametrization of the surrogate object $\mathcal{S}_{h',q'}$, i.e., a mapping $\mathcal{M}_{h',q'} : \mathcal{R}_{h',q'} \rightarrow \mathcal{S}_{h',q'}$, where $\mathcal{R}_{h',q'} \subset \mathbb{R}^{d'}$ is the parameter domain. This parametrization guarantees that for any $r \in \mathcal{R}_{h',q'}$, we have $\mathcal{M}_{h',q'}(r) \in \mathcal{S}_{h',q'}$.

To construct a mesh-based parametrization, we first define each element of the mesh $K \in \hat{\mathcal{S}}_{h',q'}$ as the image of a polynomial mapping, $\mathcal{Q}_{h',q'}^K \in [\mathcal{P}_{q'}(\Omega_\square)]^d$, applied to an idealized parent element $\Omega_\square \subset \mathbb{R}^{d'}$, i.e.,

$$K = \mathcal{Q}_{h',q'}^K(\Omega_\square), \quad (2)$$

where $\mathcal{P}_{q'}(\Omega_\square)$ is an appropriate polynomial space of degree q' over Ω_\square . The mapping is defined as

$$\mathcal{Q}_{h',q'}^K : \xi \mapsto \mathbf{x}_i^K \phi_i(\xi), \quad (3)$$

where $\{\phi_i\}_{i=1}^{n_{q'}}$ is a nodal basis of $\mathcal{P}_{q'}(\Omega_\square)$ associated with the nodes $\{\xi_1, \dots, \xi_{n_{q'}}\} \subset \Omega_\square$, $n_{q'} = \dim \mathcal{P}_{q'}(\Omega)$, and $\{\mathbf{x}_i^K, \dots, \mathbf{x}_{n_{q'}}^K\} \subset K$ are the high-order nodes of the mesh $\hat{\mathcal{S}}_{h',q'}$ associated with element $K \in \hat{\mathcal{S}}_{h',q'}$.

Next, let $\Pi_{h',q'} : \mathcal{S}_{h',q'} \rightarrow \mathbb{R}^{d'}$ be any injective mapping from the surrogate object to $\mathbb{R}^{d'}$. We use this mapping to define the parameter space $\mathcal{R}_{h',q'} \subset \mathbb{R}^{d'}$ as

$$\mathcal{R}_{h',q'} := \Pi_{h',q'}(\mathcal{S}_{h',q'}). \quad (4)$$

Furthermore, we define a mesh $\hat{\mathcal{R}}_{h',q'} \in 2^{\mathbb{R}^{d'}}$ of the parameter space by applying $\Pi_{h',q'}$ to each element of the original mesh $\hat{\mathcal{S}}_{h',q'}$, i.e.,

$$\hat{\mathcal{R}}_{h',q'} := \left\{ \Pi_{h',q'}(K) \mid K \in \hat{\mathcal{S}}_{h',q'} \right\}. \quad (5)$$

Each element $\tilde{K} \in \hat{\mathcal{R}}_{h',q'}$, where $\tilde{K} = \Pi_{h',q'}(K)$ for some $K \in \hat{\mathcal{S}}_{h',q'}$, can be written as the image of a polynomial mapping, $\mathcal{G}_{h',q'}^{\tilde{K}} \in [\mathcal{P}_{q'}(\Omega_\square)]^{d'}$, applied to the parent element Ω_\square , i.e.,

$$\tilde{K} = \mathcal{G}_{h',q'}^{\tilde{K}}(\Omega_\square). \quad (6)$$

The mapping, $\mathcal{G}_{h',q'}^{\tilde{K}}$, is defined as

$$\mathcal{G}_{h',q'}^{\tilde{K}} : \xi \mapsto \Pi_{h',q'}(\mathbf{x}_i^K) \phi_i(\xi) \quad (7)$$

and we denote its inverse as $\mathcal{H}_{h',q'}^{\tilde{K}} : \mathbb{R}^{d'} \rightarrow \mathbb{R}^{d'}$, i.e., $\mathcal{H}_{h',q'}^{\tilde{K}}(\mathcal{G}_{h',q'}^{\tilde{K}}(\xi)) = \xi$ and $\mathcal{G}_{h',q'}^{\tilde{K}}(\mathcal{H}_{h',q'}^{\tilde{K}}(r)) = r$.

Finally, the mesh-based parametrization of the surrogate object is defined as the composition of the mappings in (3) and (7)

$$\mathcal{M}_{h',q'}|_{\tilde{K}} : r \mapsto \mathcal{Q}_{h',q'}^K(\mathcal{H}_{h',q'}^{\tilde{K}}(r)) = \mathbf{x}_i^K \phi_i(\mathcal{H}_{h',q'}^{\tilde{K}}(r)). \quad (8)$$

By construction, $\mathcal{M}_{h',q'}(r) \in \mathcal{S}_{h',q'}$ for any $r \in \mathcal{R}_{h',q'}$. The construction of the mesh-based parametrization $\mathcal{M}_{h',q'}$ is illustrated in Figure 1 for a sphere surface patch ($d = 3$, $d' = 2$).

The partial derivatives of the three mappings introduced in this section will be needed to construct the first derivative of the implicit shock tracking objective and constraint in Section 3, which, in turn, will be needed to solve the constrained optimization problem using gradient-based methods. The derivative of $\mathcal{Q}_{h',q'}^K$ in (3), denoted $Q_{h',q'}^K : \Omega_\square \rightarrow \mathbb{R}^{d \times d'}$, is defined as

$$Q_{h',q'}^K : \xi \mapsto \frac{\partial \mathcal{Q}_{h',q'}^K}{\partial \xi}(\xi) = \mathbf{x}_i^K \frac{\partial \phi_i}{\partial \xi}(\xi), \quad (9)$$

where $\frac{\partial \phi_i}{\partial \xi} : \mathbb{R}^{d'} \rightarrow \mathbb{R}^{1 \times d'}$ is the derivative of the nodal basis function ϕ_i for $i = 1, \dots, n_{q'}$. The derivative of $\mathcal{G}_{h',q'}^{\tilde{K}}$ in (7), denoted $G_{h',q'}^{\tilde{K}} : \Omega_\square \rightarrow \mathbb{R}^{d' \times d'}$, is defined as

$$G_{h',q'}^{\tilde{K}} : \xi \mapsto \frac{\partial \mathcal{G}_{h',q'}^{\tilde{K}}}{\partial \xi}(\xi) = \Pi_{h',q'}(\mathbf{x}_i^K) \frac{\partial \phi_i}{\partial \xi}(\xi). \quad (10)$$

Finally, the derivative of $\mathcal{M}_{h',q'}$ in (8), denoted $M_{h',q'} : \mathcal{R}_{h',q'} \rightarrow \mathbb{R}^{d \times d'}$, is defined as

$$M_{h',q'} : r \mapsto \frac{\partial \mathcal{M}_{h',q'}}{\partial r}(r), \quad \left. \frac{\partial \mathcal{M}_{h',q'}}{\partial r} \right|_{\tilde{K}} : r \mapsto Q_{h',q'}^K(\mathcal{H}_{h',q'}^{\tilde{K}}(r)) \left[G_{h',q'}^{\tilde{K}}(\mathcal{H}_{h',q'}^{\tilde{K}}(r)) \right]^{-1}. \quad (11)$$

Remark 1. The mapping $\Pi_{h',q'}$ is non-unique. In this work, we use a simple approach to define $\Pi_{h',q'}$ by orthogonally projecting points in $\mathcal{S}_{h',q'}$ onto a predefined plane ($d' = d - 1$) or line ($d' = 1$); see [Appendix A](#) for a complete description.

Remark 2. From the elemental definition of the parametrization $\mathcal{M}_{h',q'}$ (8) and the assumption that the surrogate object $\hat{\mathcal{S}}_{h',q'}$ is globally C^0 (not C^1), the derivative of $\mathcal{M}_{h',q'}$ is discontinuous across element

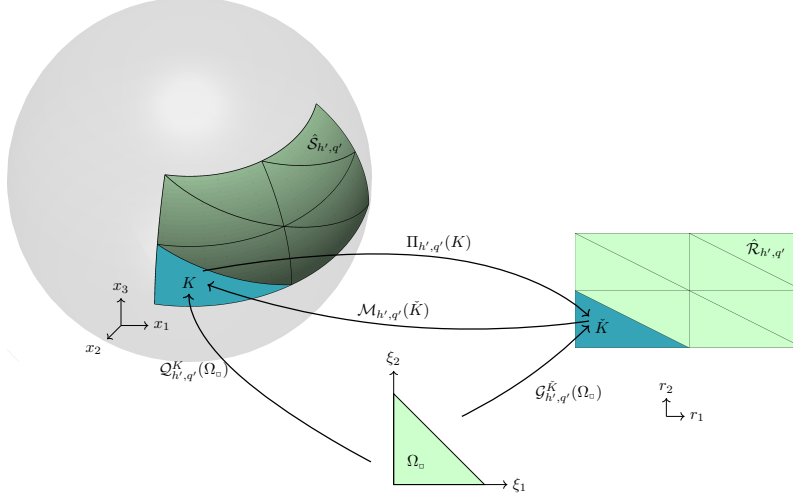


Figure 1: Schematic of the surface mesh parametrization $\mathcal{M}_{h',q'}$ built as the composition of $\mathcal{Q}_{h',q'}^K$ and $\mathcal{G}_{h',q'}^{\tilde{K}}$ mappings (Section 2.1) for a surface patch of a sphere in $d = 3$ dimensions ($d' = 2$).

boundaries. In this work, we investigate two approaches to obtain a single value of $M_{h',q'}(r)$ for any $r \in \bigcap_{\tilde{K} \in \mathcal{X}_r} \tilde{K}$, where $\mathcal{X}_r \subset \hat{\mathcal{R}}_{h',q'}$ is the collection of all elements containing the point r . The simplest and most efficient option applies (11) for a single, arbitrary $\tilde{K} \in \mathcal{X}_r$. A more accurate (relative to the derivative of a parametrization of the true, not surrogate, surface) but more expensive approach averages the derivative over all elements in \mathcal{X}_r , i.e.,

$$\frac{\partial \mathcal{M}_{h',q'}}{\partial r} : r \mapsto \frac{1}{|\mathcal{X}_r|} \sum_{\tilde{K} \in \mathcal{X}_r} \mathcal{Q}_{h',q'}^{\tilde{K}}(\mathcal{H}_{h',q'}^{\tilde{K}}(r)) \left[\mathcal{G}_{h',q'}^{\tilde{K}}(\mathcal{H}_{h',q'}^{\tilde{K}}(r)) \right]^{-1}. \quad (12)$$

While the definition in (12) is more accurate than (11), the implementation in (11) is easier and more efficient because it only requires finding a single element $\tilde{K} \in \hat{\mathcal{R}}_{h',q'}$ containing r . Both methods converge to the derivative of a parametrization of the true surface as the mesh is refined $h' \rightarrow 0$, especially for higher polynomial degrees q' . In this work, we use the more accurate implementation in (12), aided by our efficient search algorithm in Section 2.3.

2.2. Boundary-preserving, mesh-based parametrization of computational mesh

Implicit shock tracking dynamically moves the nodes of a computational mesh to align element faces with non-smooth flow features. While internal nodes can move freely, boundary nodes must always remain on their original boundaries. Allowing nodes to move on or off boundaries would lead to faces that straddle multiple boundaries. This would make it impossible to assign a single boundary condition to such faces. Furthermore, complex geometries are often non-smooth across boundary surfaces so allowing a face to straddle multiple boundaries would lead to oscillations in the high-order element. In this section we use the mesh-based parametrizations (Section 2.1) to parametrize all nodes of a computational mesh in such a way that they are guaranteed to remain on their original boundaries. Such a parametrization was introduced in [41, 14, 8] for domains with planar boundaries and for domains with curved boundaries assuming an explicit parametrization of the curved boundaries was available. Our approach only requires a mesh of the boundaries and their intersections.

Consider a computational domain $\Omega \subset \mathbb{R}^d$ with smooth boundaries $\partial\Omega_i \subset \mathbb{R}^d$ for $i = 1, \dots, N_b$. Let $\hat{\Omega}_{h,q} \in 2^{\mathbb{R}^d}$ be a high-order mesh of Ω with mesh size parameter h and polynomial degree q . This will be the mesh used for the implicit shock tracking simulation in Sections 3-4. We assume the mesh $\hat{\Omega}_{h,q}$ is built from conforming Lagrangian finite elements to ensure the surrogate domain

$$\Omega_{h,q} := \bigcup_{K \in \hat{\Omega}_{h,q}} K \quad (13)$$

is globally C^0 , and let $\{\mathbf{X}_I\}_{I=1}^{N_x} \subset \mathbb{R}^d$ be the nodes (global numbering) associated with the Lagrange elements. Next, define $B_i \in 2^{\{1, \dots, N_b\}}$ as the collection of boundaries on which node i lies for $i = 1, \dots, N_x$, i.e., $I \notin B_i \implies \mathbf{X}_i \notin \partial\Omega_I$. Let \mathcal{I}_s denote the collection of all nodes that lie on exactly s boundaries, i.e.,

$$\mathcal{I}_s := \{i \in \{1, \dots, N_x\} \mid |B_i| = s\}, \quad (14)$$

for $s = 0, 1, \dots, N_b$, where $|S|$ is the cardinality of the set S . Each $i \in \{1, \dots, N_x\}$ lies in exactly one of the sets $\mathcal{I}_0, \dots, \mathcal{I}_{N_b}$.

Next, we construct a mesh-based parametrization of the computational mesh $\hat{\Omega}_{h,q}$ as a parametrization of its nodal coordinates. Let $\hat{\mathcal{S}}_{h',q'}^S$ be a high-order mesh of the intersection of the boundaries in $S \in 2^{\{1, \dots, N_b\}}$, i.e., $\bigcap_{s \in S} \partial\Omega_s$, with mesh size parameter h' and polynomial degree q' , and let $\mathcal{S}_{h',q'}^S = \bigcup_{K \in \hat{\mathcal{S}}_{h',q'}^S} K$ be the surrogate intersection. We call $\hat{\mathcal{S}}_{h',q'}^S$ a *geometry* mesh in the remainder; see Remark 4 for approaches to construct $\hat{\mathcal{S}}_{h',q'}^S$. Then, let $\mathcal{M}_{h',q'}^S$ (8) be a mesh-based parametrization of the intersection of the boundaries in S based on the geometry mesh $\hat{\mathcal{S}}_{h',q'}^S$ with parameter domain $\mathcal{R}_{h',q'}^S$ and mesh $\hat{\mathcal{R}}_{h',q'}^S$ (5), and physical-to-parameter mapping $\Pi_{h',q'}^S$ (4). From these definitions, the domain of the computational mesh parametrization $\mathcal{Y}_{h',q'} \subset \mathbb{R}^{N_y}$ is

$$\mathcal{Y}_{h',q'} := \mathcal{R}_{h',q'}^{B_1} \times \dots \times \mathcal{R}_{h',q'}^{B_{N_x}}, \quad (15)$$

where $\dim \mathcal{R}_{h',q'}^{B_i} = \max\{d - s, 0\}$ for $i \in \mathcal{I}_s$ (Remark 5), which makes the embedding dimension $N_y = \sum_{s=0}^{d-1} (d - s) |\mathcal{I}_s|$. Owing to the form of the parameter domain (15), any $\mathbf{y} \in \mathcal{Y}_{h',q'}$ has a nodal structure $\mathbf{y} = (\mathbf{y}_1, \dots, \mathbf{y}_{N_x})$ where $\mathbf{y}_i \in \mathcal{R}_{h',q'}^{B_i} \subset \mathbb{R}^{\max\{d-s, 0\}}$ for $i \in \mathcal{I}_s$. Finally, we define the mesh-based parametrization of the computational mesh $\hat{\Omega}_{h,q}$ as $\phi : \mathcal{Y}_{h',q'} \rightarrow \mathbb{R}^{dN_x}$, $\phi : \mathbf{y} \mapsto (\phi_1(\mathbf{y}_1), \dots, \phi_{N_x}(\mathbf{y}_{N_x}))$. The nodal parametrization $\phi_i : \mathcal{R}_{h',q'}^{B_i} \rightarrow \mathbb{R}^d$ is defined as

$$\phi_i : \mathbf{y}_i \mapsto \begin{cases} \mathbf{y}_i & i \in \mathcal{I}_0 \\ \mathcal{M}_{h',q'}^{B_i}(\mathbf{y}_i) & i \in \mathcal{I}_1 \cup \dots \cup \mathcal{I}_{d-1} \\ \mathbf{X}_i & i \in \mathcal{I}_d \cup \dots \cup \mathcal{I}_{N_b} \end{cases} \quad (16)$$

for $i = 1, \dots, N_x$. We call $\mathbf{y} \in \mathcal{Y}_{h',q'}$ the unconstrained degrees of freedom because, for any $\mathbf{y}_i \in \mathcal{R}_{h',q'}^{B_i}$, $\mathbf{x}_i = \phi_i(\mathbf{y}_i) \in \mathbb{R}^d$ is guaranteed, by construction, to lie on the same (surrogate) boundaries as $\mathbf{X}_i \in \mathbb{R}^d$, i.e., $\mathbf{x}_i \in \mathcal{S}_{h',q'}^{B_i}$. The Jacobian of the mesh parametrization, $\frac{\partial \phi}{\partial \mathbf{y}} : \mathbb{R}^{N_y} \rightarrow \mathbb{R}^{dN_x \times N_y}$, is obtained from direct differentiation of (16) to yield

$$\frac{\partial \phi}{\partial \mathbf{y}} : \mathbf{y} \mapsto \begin{bmatrix} \frac{\partial \phi_1}{\partial \mathbf{y}_1}(\mathbf{y}) & & & \\ & \ddots & & \\ & & \frac{\partial \phi_{N_x}}{\partial \mathbf{y}_{N_x}}(\mathbf{y}) & \\ & & & \end{bmatrix}, \quad \frac{\partial \phi_i}{\partial \mathbf{y}_i} : \mathbf{y}_i \mapsto \begin{cases} I_{d \times d} & i \in \mathcal{I}_0 \\ M_{h',q'}^{B_i}(\mathbf{y}_i) & i \in \mathcal{I}_1 \cup \dots \cup \mathcal{I}_{d-1} \\ \mathbf{0}_{d \times 0} & i \in \mathcal{I}_d \cup \dots \cup \mathcal{I}_{N_b}, \end{cases} \quad (17)$$

where $\frac{\partial \phi_i}{\partial \mathbf{y}_i}(\mathbf{y}_i) \in \mathbb{R}^{d \times \max\{d-s, 0\}}$ for $i \in \mathcal{I}_s$ and $M_{h',q'}^S = \frac{\partial \mathcal{M}_{h',q'}^S}{\partial \mathbf{r}}$ is the derivative of the mesh-based parametrization $\mathcal{M}_{h',q'}^S$ (11).

Remark 3. Any non-smooth features on $\partial\Omega$, the boundary of the computational domain Ω , are assumed to lie at the intersection of distinct boundaries, which means each boundary itself is smooth. This is standard practice in both CAD modeling and mesh generation and therefore does not increase the burden of constructing mesh-based parametrizations.

Remark 4. The geometry mesh, $\hat{\mathcal{S}}_{h',q'}$, can be extracted from the computational mesh $\hat{\Omega}_{h,q}$, in which case, $h' = h$ and $q' = q$. It can also easily be built with different resolution ($h' \neq h$, $q' \neq q$) than the computational mesh and can be defined without a volume mesh. A straightforward strategy to build a geometry mesh is to create a conforming mesh of all boundaries with sufficient resolution (h' and q') for the geometry of the vehicle without regard to the flow conditions or features expected. This is usually a byproduct of the computational mesh $\hat{\Omega}_{h,q}$ generation process so it is not an additional burden in the workflow. The geometry mesh of all

boundaries and their intersections can be extracted directly from this surface mesh.

Remark 5. The subscript s in \mathcal{I}_s denotes the number of constraints imposed on the nodes in the set, which means node $i \in \mathcal{I}_s$ will lie on a geometric object of dimension $\max\{d-s, 0\}$. For example, in $d = 3$, any node in \mathcal{I}_0 is unconstrained in three-dimensional volume, any node in \mathcal{I}_1 lies on exactly one surface (intrinsic dimension $d' = 2$), any node in \mathcal{I}_2 lies at the intersection of two surfaces (a curve with intrinsic dimension $d' = 1$), and any node in $\mathcal{I}_3 \cup \dots \cup \mathcal{I}_{N_b}$ lies at the intersection of three or more surfaces (a point with intrinsic dimension $d' = 0$). This approach could overconstrain node motion because it is possible that a completely smooth surfaces is arbitrarily split into two boundaries. In this setting, nodes would be required to remain on the curve at the intersection of these two boundaries. The proposed approach could be modified to allow nodes to move between boundaries if the transition between them is smooth and they use the same boundary condition. However, there is rarely a practical benefit of this approach due to its additional cost and the increased software complexity.

Remark 6. The mapping from unconstrained degrees of freedom (\mathbf{y}) to nodal coordinates (\mathbf{x}) is well-defined; however, for most values of $\mathbf{x} \in \mathbb{R}^{dN_x}$, it is not possible to define $\mathbf{y} \in \mathbb{R}^{N_y}$ such that $\mathbf{x} = \phi(\mathbf{y})$ (i.e., invert the mapping ϕ). We define a pseudo-inverse of ϕ as $\phi^\dagger : \mathbb{R}^{dN_x} \rightarrow \mathbb{R}^{N_y}$, where $\phi^\dagger : \mathbf{x} \mapsto (\phi_1^\dagger(\mathbf{x}_1), \dots, \phi_{N_x}^\dagger(\mathbf{x}_{N_x}))$ and $\phi_i^\dagger : \mathbb{R}^d \mapsto \mathbb{R}^{\max\{d-s, 0\}}$ with $i \in \mathcal{I}_s$ for $i = 1, \dots, N_x$ is defined as

$$\phi_i^\dagger(\mathbf{x}) = \begin{cases} \mathbf{x}_i & i \in \mathcal{I}_0 \\ \Pi_{h',q'}^{B_i}(\mathbf{x}_i) & i \in \mathcal{I}_1 \cup \dots \cup \mathcal{I}_{d-1} \\ \mathbf{X}_i & i \in \mathcal{I}_d \cup \dots \cup \mathcal{I}_{N_b}. \end{cases} \quad (18)$$

2.3. Efficient element search in high-order mesh

Evaluation of $\mathcal{M}_{h',q'}(r)$ (8) or $M_{h',q'}(r)$ for any $r \in \mathcal{R}_{h',q'}$ requires a search through the mesh $\hat{\mathcal{R}}_{h',q'}$ to find the element(s) $\check{K} \in \hat{\mathcal{R}}_{h',q'}$ in which r lies. The condition $r \in \check{K}$ is difficult to check if \check{K} is a curved element; however, $r \in \check{K}$ if and only if $\xi \in \Omega_\square$ where $r = \mathcal{G}_{h',q'}^{\check{K}}(\xi)$. The later condition $\xi \in \Omega_\square$ is easy to check because Ω_\square is a straight-sided parent element, but requires inversion of the element mapping, which can be expensive. Furthermore, we must search through each element $\check{K} \in \hat{\mathcal{R}}_{h',q'}$ until one (or more) containing $r \in \mathcal{R}_{h',q'}$ is found. This strategy can be accelerated by eliminating elements that do not need to be checked based on the location of $r \in \mathcal{R}_{h',q'}$ [20, 25]; however, this can be tricky for curved elements. We propose a variant of the search acceleration techniques in [25] specialized for high-order (curved) meshes. The algorithm is defined for the mesh $\hat{\mathcal{R}}_{h',q'}$ of the domain $\mathcal{R}_{h',q'}$ with element mapping $\mathcal{G}_{h',q'}^{\check{K}}$ because the notation is established; however, it could be applied to any high-order mesh of a given domain.

Given a point $r \in \mathcal{R}_{h',q'}$, we wish to find all elements $\check{K} \in \hat{\mathcal{R}}_{h',q'}$ such that $r \in \check{K}$. First, we distribute points in each element of the mesh $\hat{\mathcal{R}}_{h',q'}$. Let $\mathcal{D}_{\check{K}} \subset \check{K}$ with $|\mathcal{D}_{\check{K}}| = n$ denote this set of points (Remark 7) and let $\mathcal{D} \subset \mathcal{R}_{h',q'}$ be the union of all points, i.e.,

$$\mathcal{D} = \bigcup_{\check{K} \in \hat{\mathcal{R}}_{h',q'}} \mathcal{D}_{\check{K}}. \quad (19)$$

Next, we define the k th nearest point of $r \in \mathcal{R}_{h',q'}$ as $y_r^k \in \mathcal{D}$, where

$$y_r^k := \arg \min_{y \in \mathcal{D} \setminus \{y_r^1, \dots, y_r^{k-1}\}} \|r - y\| \quad (20)$$

for $k > 0$ (Remark 8). We associate the nearest points with a collection of elements (each point may lie in multiple elements), $\mathcal{J}_r^k \subset \hat{\mathcal{R}}_{h',q'}$, where

$$\mathcal{J}_r^k := \left\{ \check{K} \in \hat{\mathcal{R}}_{h',q'} \mid y_r^k \in \mathcal{D}_{\check{K}} \right\} \setminus \bigcup_{k'=1}^{k-1} \mathcal{J}_r^{k'}. \quad (21)$$

The elements of the sets $\mathcal{J}_r^1, \dots, \mathcal{J}_r^{k-1}$ are not included in \mathcal{J}_r^k to avoid searching for the point r in the same element multiple times. Finally, we build the collection of elements containing r as $\mathcal{K}_r := \mathcal{K}_r^1 \cup \dots \cup \mathcal{K}_r^k$,

where $\mathcal{K}_r^k \subset \hat{\mathcal{R}}_{h',q'}$ is defined as

$$\mathcal{K}_r^k := \left\{ \check{K} \in \mathcal{J}_r^k \mid \xi \in \Omega_\square \text{ where } r = \mathcal{G}_{h',q'}^{\check{K}}(\xi) \right\}. \quad (22)$$

That is, the set \mathcal{K}_r^k is built from inverting the element mapping of each element in \mathcal{J}_r^k at r and determining if that new point lies in Ω_\square . As written, this method will find all elements in $\mathcal{J}_r^1 \cup \dots \cup \mathcal{J}_r^k$ containing r . In practice, k is used as a safeguard to prevent the search from including all elements of the mesh (we take $k = 5$ in this work). If we only seek *one* element containing r , the sets $\mathcal{K}_r^1, \dots, \mathcal{K}_r^k$ are built sequentially and the search is terminated after the first element containing r is found (usually during the construction of \mathcal{K}_r^1). The proposed acceleration search algorithm is demonstrated in Figure 2.

Remark 7. *The point distributions, $\mathcal{D}_{\check{K}}$, can be constructed by first defining a distribution in the parent element $\mathcal{D}_\square \subset \Omega_\square$ and using the element transformation to map them to the physical element $\check{K} \in \hat{\mathcal{R}}_{h',q'}$, i.e.,*

$$\mathcal{D}_{\check{K}} = \left\{ \mathcal{G}_{h',q'}^{\check{K}}(\xi) \mid \xi \in \mathcal{D}_\square \right\}. \quad (23)$$

Remark 8. *The nearest neighbors y_r^j for $j = 1, \dots, k$ can be efficiently found using binary trees. In this work we use the implementation in the `NearestNeighbors.jl` Julia package [4].*

Remark 9. *This algorithm is efficient because the point r almost always lies in one of the elements of \mathcal{J}_r^1 . In practice, this only fails when n is too small or when the mesh is highly skewed. In those cases, the search must proceed to \mathcal{J}_r^2 . We have not encountered a situation, in practice, where the search must continue to \mathcal{J}_r^3 to find the first element containing r .*

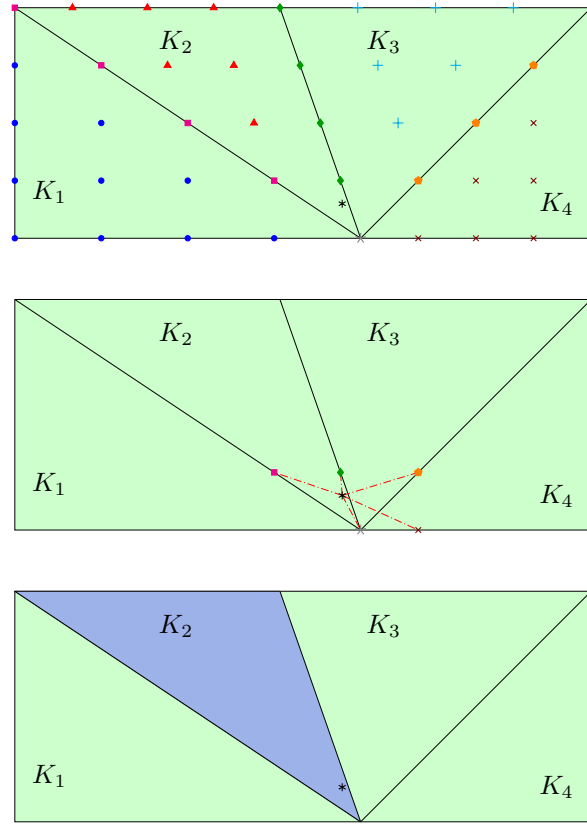


Figure 2: Illustration of search algorithm (Section 2.3) for element in which a point (*) lies. *Top*: The point distributions \mathcal{D}_{K_1} ($\bullet, \blacksquare, *$), \mathcal{D}_{K_2} ($\blacktriangle, \blacklozenge, \blacktriangleright, *$), \mathcal{D}_{K_3} ($\color{cyan}+, \color{cyan}\blacklozenge, \color{cyan}\blacktriangleright, *$), \mathcal{D}_{K_4} ($\times, \color{orange}\bullet, *$). *Middle*: The $k = 5$ nearest points to the query point r (*): y_r^1 ($\color{green}\blacklozenge$), y_r^2 ($\color{pink}\blacktriangleright$), y_r^3 ($\color{purple}\blacklozenge$), y_r^4 ($\color{orange}\bullet$), y_r^5 ($\color{red}\blacktriangleright$). The nearest points correspond to element sets $\mathcal{J}_r^1 = \{K_2, K_3\}$, $\mathcal{J}_r^2 = \{K_1, K_4\}$, $\mathcal{J}_r^3 = \emptyset$, $\mathcal{J}_r^4 = \emptyset$, $\mathcal{J}_r^5 = \emptyset$. *Bottom*: The elements identified containing r (*): $\mathcal{K}_r^1 = \{K_2\}$, $\mathcal{K}_r^2 = \emptyset$, $\mathcal{K}_r^3 = \emptyset$, $\mathcal{K}_r^4 = \emptyset$, $\mathcal{K}_r^5 = \emptyset$.

3. Implicit shock tracking for shock-dominated flow over complex domains

In this section we formulate the High-Order Implicit Shock Tracking method (Section 3.3) from a discontinuous Galerkin discretization (Section 3.2) of a general system of conservation laws posed on a fixed reference domain so domain mappings (nodal coordinates after discretization) appear explicitly in the flux and source terms (Section 3.1).

3.1. Governing equations

Consider a general system of m hyperbolic partial differential equations posed in the domain $\Lambda \subset \mathbb{R}^d$

$$\nabla \cdot F(U) = S(U), \quad (24)$$

where $x = (x_1, \dots, x_d) \in \Lambda$ is the coordinate, $U : \Lambda \rightarrow \mathbb{R}^m$ is the conservative state implicitly defined as the solution to (24), $F : \mathbb{R}^m \rightarrow \mathbb{R}^{m \times d}$ with $F : W \mapsto F(W)$ is the physical flux function, $S : \mathbb{R}^m \rightarrow \mathbb{R}^m$ is the physical source term, $(\nabla \cdot \psi)$ is the divergence operator on the domain Λ defined as $(\nabla \cdot \psi)_i := \partial_{x_j} \psi_{ij}$ (summation implied on repeated index), and $\partial\Lambda$ is the boundary of the spatial domain (with appropriate boundary conditions prescribed). In general, the solution $U(x)$ may contain discontinuities, in which case, the conservation law (24) holds away from the discontinuities and the Rankine-Hugoniot conditions hold at discontinuities.

Next, we write the physical domain Λ as a transformation of a fixed reference domain $\Omega \subset \mathbb{R}^d$ (the computational domain introduced in Section 2.2), i.e., $\Lambda = \Xi(\Omega)$, where $\Xi : \Omega \rightarrow \Lambda$ with $\Xi : \bar{x} \mapsto \Xi(\bar{x})$ is any diffeomorphism from the reference domain to the physical domain. Then we recast the conservation law (24) on the physical domain as a transformed conservation law on the reference domain so the transformation appears explicitly in the flux and source terms [27, 39], i.e.,

$$\bar{\nabla} \cdot \bar{F}(\bar{U}; \partial_{\bar{x}} \Xi) = \bar{S}(\bar{U}; \det(\partial_{\bar{x}} \Xi)), \quad (25)$$

where $\bar{U} : \Omega \rightarrow \mathbb{R}^m$ is the solution of the transformed conservation law, $\bar{F} : \mathbb{R}^m \times \mathbb{R}^{d \times d} \rightarrow \mathbb{R}^{m \times d}$ and $\bar{S} : \mathbb{R}^m \times \mathbb{R} \rightarrow \mathbb{R}^m$ are the transformed flux function and source term, respectively, and $\bar{\nabla} \cdot$ is the divergence operator in the reference domain Ω defined as $(\bar{\nabla} \cdot \psi)_i = \partial_{\bar{x}_j} \psi_{ij}$. The reference domain quantities are defined in terms of the corresponding physical domain quantities as [39]

$$\bar{U}(\bar{x}) = U(\Xi(\bar{x})), \quad \bar{F} : (\bar{W}; \Theta) \mapsto (\det \Theta) \mathcal{F}(\bar{W}) \Theta^{-T}, \quad \bar{S} : (\bar{W}; q) \mapsto qS(\bar{W}). \quad (26)$$

3.2. Discontinuous Galerkin discretization

We discretize the transformed conservation law (25) with a discontinuous Galerkin method [13] with high-order piecewise polynomials spaces used to approximate the state \bar{U} and domain mapping Ξ . To this end, let $\hat{\Omega}_{h,q}$ represent a discretization of the reference domain Ω into non-overlapping, potentially curved, computational elements (the computational mesh introduced in Section 2.2) and let $\Omega_{h,q}$ be the surrogate domain (13). To establish the finite-dimensional DG formulation, we introduce the DG approximation (trial) space of discontinuous piecewise polynomials associated with the mesh $\hat{\Omega}_{h,q}$

$$\mathcal{V}_{h,q}^p := \left\{ v \in [L^2(\Omega_{h,q})]^m \mid v|_{\bar{K}} \in [\mathcal{P}_p(\bar{K})]^m, \forall \bar{K} \in \hat{\Omega}_{h,q} \right\}, \quad (27)$$

Furthermore, we define the space of globally continuous piecewise polynomials of degree q associated with the mesh $\hat{\Omega}_{h,q}$ as

$$\mathcal{W}_{h,q} := \left\{ v \in C^0(\Omega_{h,q}) \mid v|_{\bar{K}} \in \mathcal{P}_q(\bar{K}), \forall \bar{K} \in \hat{\Omega}_{h,q} \right\} \quad (28)$$

and discretize the domain mapping with the corresponding vector-valued space $[\mathcal{W}_{h,q}]^d$. With these definitions, the DG variational problem is: given $\Xi_h \in [\mathcal{W}_{h,q}]^d$, find $\bar{U}_h \in \mathcal{V}_{h,q}^p$ such that for all $\bar{\psi}_h \in \mathcal{V}_{h,q}^p$, we have

$$r_h^{p',p}(\bar{\psi}_h, \bar{U}_h; \partial_{\bar{x}} \Xi_h) = 0 \quad (29)$$

where $p' \geq p$ and the global residual function $r_h^{p',p} : \mathcal{V}_{h,q}^{p'} \times \mathcal{V}_{h,q}^p \times [\mathcal{W}_{h,q}]^d \rightarrow \mathbb{R}$ is defined in terms of elemental residuals $r_{\bar{K}}^{p',p} : \mathcal{V}_{h,q}^{p'} \times \mathcal{V}_{h,q}^p \times [\mathcal{W}_{h,q}]^d \rightarrow \mathbb{R}$ as

$$r_h^{p',p} : (\bar{\psi}_h, \bar{W}_h; \Theta_h) \mapsto \sum_{\bar{K} \in \bar{\Omega}_{h,q}} r_{\bar{K}}^{p',p}(\bar{\psi}_h, \bar{W}_h; \Theta_h). \quad (30)$$

The elemental residuals come directly from a standard DG formulation applied to the transformed conservation law in (25)

$$\begin{aligned} r_{\bar{K}}^{p',p} : (\bar{\psi}_h, \bar{W}_h; \Theta_h) \mapsto & \int_{\partial \bar{K}} \bar{\psi}_h \cdot \bar{\mathcal{H}}(W_h^+, W_h^-, \bar{n}_h; \Theta_h) dS \\ & - \int_{\bar{K}} \bar{F}(W_h; \Theta_h) : \bar{\nabla} \bar{\psi}_h dV \\ & - \int_{\bar{K}} \bar{\psi}_h \cdot \bar{S}(W_h; \det \Theta_h) dV, \end{aligned} \quad (31)$$

where $\bar{\eta}_h : \partial \bar{K} \mapsto \mathbb{R}^d$ is the outward unit normal to an element $\bar{K} \in \bar{\Omega}_{h,q}$, \bar{W}_h^+ (\bar{W}_h^-) denotes the interior (exterior) trace of $\bar{W}_h \in \mathcal{V}_{h,q}^p$ to the element, and $\bar{\mathcal{H}}$ is the transformed numerical (Roe) flux function [30, 41].

Finally, we introduce a basis for the test space ($\mathcal{V}_{h,q}^{p'}$), trial space ($\mathcal{V}_{h,q}^p$), and domain mapping space ($[\mathcal{W}_{h,q}]^d$) to reduce the weak formulation in (29)-(31) to a system of nonlinear algebraic equations. In the case where $p = p'$, we have

$$\mathbf{r} : \mathbb{R}^{N_u} \times \mathbb{R}^{dN_x} \rightarrow \mathbb{R}^{N_u}, \quad \mathbf{r} : (\mathbf{u}, \mathbf{x}) \mapsto \mathbf{r}(\mathbf{u}, \mathbf{x}), \quad (32)$$

where $N_u = \dim(\mathcal{V}_{h,q}^p)$ and $N_x = \dim(\mathcal{W}_{h,q})$, which is the residual of a standard DG method. The algebraic state $\mathbf{u} \in \mathbb{R}^{N_u}$ contains the coefficients of the flow solution in the chosen basis and $\mathbf{x} \in \mathbb{R}^{dN_x}$ contains the nodal coordinates of the physical mesh because a Lagrangian basis is used for the continuous $\mathcal{W}_{h,q}$ space. Next, we define the algebraic enriched residual associated with a test space of degree $p' > p$ ($p' = p + 1$ in this work) as

$$\mathbf{R} : \mathbb{R}^{N_u} \times \mathbb{R}^{dN_x} \rightarrow \mathbb{R}^{N'_u}, \quad \mathbf{R} : (\mathbf{u}, \mathbf{x}) \mapsto \mathbf{R}(\mathbf{u}, \mathbf{x}), \quad (33)$$

where $N'_u = \dim(\mathcal{V}_{h,q}^{p'})$, which will be used to construct the implicit shock tracking objective function.

3.3. Implicit shock tracking formulation

The HOIST method [41] simultaneously computes the discrete solution of the conservation law and the nodal coordinates of the mesh that causes element faces to align with discontinuities. This is achieved through a fully discrete, full space PDE-constrained optimization formulation with the optimization variables taken to be the discrete flow solution (\mathbf{u}) and nodal coordinates of the mesh (\mathbf{x}). The nodal coordinates are constrained to ensure all nodes remain on their original boundaries using the mesh-based parametrization of Section 2.2. This is accomplished by requiring the nodal coordinates be in the image of the mesh-based parametrization ϕ , i.e., there exists $\mathbf{y} \in \mathcal{Y}_{h',q'}$ such that $\mathbf{x} = \phi(\mathbf{y})$. This leads to the following formulation of the HOIST method

$$(\mathbf{u}^*, \mathbf{y}^*) := \arg \min_{\mathbf{u} \in \mathbb{R}^{N_u}, \mathbf{y} \in \mathbb{R}^{N_y}} f(\mathbf{u}, \mathbf{y}) \quad \text{subject to: } \mathbf{c}(\mathbf{u}, \mathbf{y}) = \mathbf{0}, \quad (34)$$

where $f : \mathbb{R}^{N_u} \times \mathbb{R}^{N_y} \rightarrow \mathbb{R}$ is the objective function, $\mathbf{c} : \mathbb{R}^{N_u} \times \mathbb{R}^{N_y} \rightarrow \mathbb{R}^{N_u}$ is the constraint function, and the nodal coordinates of the aligned mesh are $\mathbf{x}^* = \phi(\mathbf{y}^*)$. The objective function is composed of two terms as

$$f : (\mathbf{u}, \mathbf{y}) \mapsto f_{\text{err}}(\mathbf{u}, \mathbf{y}) + \kappa^2 f_{\text{msh}}(\mathbf{y}), \quad (35)$$

which balances alignment of the mesh with non-smooth features and the quality of the elements and $\kappa \in \mathbb{R}_{\geq 0}$ is the mesh penalty parameter. The mesh alignment term, $f_{\text{err}} : \mathbb{R}^{N_u} \times \mathbb{R}^{N_y} \rightarrow \mathbb{R}$, is taken to be the norm of the enriched DG residual

$$f_{\text{err}} : (\mathbf{u}, \mathbf{y}) \mapsto \frac{1}{2} \|\mathbf{R}(\mathbf{u}, \phi(\mathbf{y}))\|_2^2. \quad (36)$$

To ensure elements of the discontinuity-aligned mesh are high-quality, we define the mesh distortion term, $f_{\text{msh}} : \mathbb{R}^{N_y} \rightarrow \mathbb{R}$, as

$$f_{\text{msh}} : \mathbf{y} \mapsto \frac{1}{2} \|\mathbf{R}_{\text{msh}}(\phi(\mathbf{y}))\|_2^2, \quad (37)$$

where $\mathbf{R}_{\text{msh}} : \mathbb{R}^{N_y} \rightarrow \mathbb{R}^{|\hat{\Omega}_{h,q}|}$ is the elementwise mesh distortion with respect to an ideal element [41, 19, 29]. Finally, the constraint is the standard DG residual to ensure the HOIST method inherits the desirable properties of DG, i.e.,

$$\mathbf{c} : (\mathbf{u}, \mathbf{y}) \mapsto \mathbf{r}(\mathbf{u}, \phi(\mathbf{y})). \quad (38)$$

The constrained optimization problem in (34) is solved using the sequential quadratic programming (SQP) method in [41, 14]. This gradient-based optimizer requires the derivatives of the objective and constraint with respect to both \mathbf{u} and \mathbf{y} . The \mathbf{u} derivatives are straightforward and described in [41, 14], whereas the \mathbf{y} derivatives involve the Jacobian of the mesh-based parametrization ϕ . The \mathbf{y} -gradient of the objective function, $\nabla_{\mathbf{y}} f : \mathbb{R}^{N_u} \times \mathbb{R}^{N_y} \mapsto \mathbb{R}^{N_y}$, takes the form

$$\nabla_{\mathbf{y}} f : (\mathbf{u}, \mathbf{y}) \mapsto \frac{\partial \phi}{\partial \mathbf{y}}(\mathbf{y})^T \frac{\partial \mathbf{R}}{\partial \mathbf{x}}(\mathbf{y}, \phi(\mathbf{y}))^T \mathbf{R}(\mathbf{u}, \phi(\mathbf{y})) \quad (39)$$

and the \mathbf{y} -Jacobian of the constraint function, $\frac{\partial \mathbf{c}}{\partial \mathbf{y}} : \mathbb{R}^{N_u} \times \mathbb{R}^{N_y} \mapsto \mathbb{R}^{N_u \times N_y}$, is

$$\frac{\partial \mathbf{c}}{\partial \mathbf{y}}(\mathbf{u}, \mathbf{y}) \mapsto \frac{\partial \mathbf{r}}{\partial \mathbf{x}}(\mathbf{u}, \phi(\mathbf{y})) \frac{\partial \phi}{\partial \mathbf{y}}(\mathbf{y}), \quad (40)$$

where $\frac{\partial \phi}{\partial \mathbf{y}}$ is the Jacobian of the mesh-based parametrization defined in (17).

Remark 10. *The condition $\mathbf{y} \in \mathcal{Y}_{h',q'}$ was relaxed to $\mathbf{y} \in \mathbb{R}^{N_y}$ in (34) because any $\mathbf{y} \notin \mathcal{Y}_{h',q'}$ would lead to a mesh $\mathbf{x} = \phi(\mathbf{y})$ with inverted elements, which would cause $f_{\text{msh}}(\mathbf{x})$ to blow up and be rejected by the optimizer.*

4. Numerical experiments

In this section we provide two concrete examples of the mesh-based parametrization that show the surrogate objects being parametrized rapidly approach the true object (Section 4.1). We also provide two examples that demonstrate mesh-based parametrizations integrate cleanly into implicit shock tracking, effectively lead to shock-aligned grids even when the shocks intersect the boundary, and do not impede convergence of the optimization solver (Section 4.2-4.3). Finally, we show mesh-based parametrizations can be used to easily slide nodes along complex geometries and surface intersections using a relevant hypersonic vehicle, the sliced cone flap (Section 4.4).

4.1. Surface approximation quality of mesh-based parametrizations

In this section we demonstrate the accuracy of mesh-based parametrization and its derivative with respect to known geometries: a two-dimensional Gaussian bump (Section 4.1.1) and quarter sphere (Section 4.1.2). Despite being a parametrization of a globally C^0 surrogate surface, the mesh-based parametrization accurately represent the underlying surfaces and its normals, especially when the geometry mesh is refined (small h' or large q').

Let $\mathcal{S} \subset \mathbb{R}^d$ be the true surface of interest and $\mathcal{M} : \mathcal{R} \rightarrow \mathcal{S}$ be a parametrization of the surface with parameter domain $\mathcal{R} \subset \mathbb{R}^d$. We quantify the error in the mesh-based parametrization $\mathcal{M}_{h',q'}$ and its derivative $M_{h',q'}$ using the normalized error metrics, $E : \mathcal{R}_{h',q'} \rightarrow \mathbb{R}_{\geq 0}$ and $E_{\partial} : \mathcal{R}_{h',q'} \rightarrow \mathbb{R}_{\geq 0}$, defined as

$$E : r \mapsto \frac{\|\mathcal{M}_{h',q'}(r) - \mathcal{M}(r)\|}{\sup_{r' \in \mathcal{R}} \|\mathcal{M}(r')\|}, \quad E_{\partial} : r \mapsto \frac{\|M_{h',q'}(r) - \frac{\partial \mathcal{M}(r)}{\partial r}\|}{\sup_{r' \in \mathcal{R}} \|\frac{\partial \mathcal{M}(r')}{\partial r}\|}. \quad (41)$$

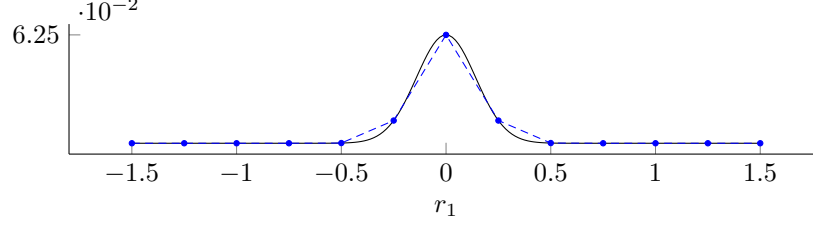


Figure 3: The true surface \mathcal{S} (—) for the Gaussian bump and a surrogate surface $\mathcal{S}_{h',q'}$ with $h' = 0.25$, $q' = 1$ (-·-·).

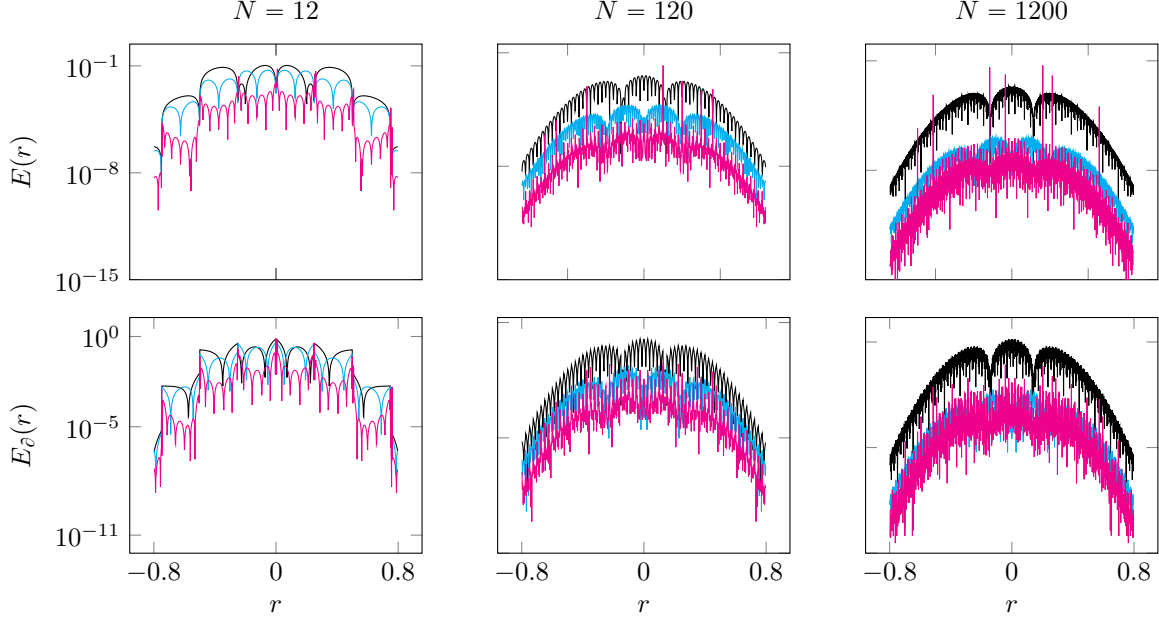


Figure 4: The error in the mesh-based parametrization (*top*) and its derivative (*bottom*) of the Gaussian bump for three h -refinement levels (*columns*) for polynomial degrees $q' = 1$ (—), $q' = 2$ (—), and $q' = 6$ (—). The r limits are restricted to $(-0.8, 0.8)$ because the errors in the near-constant region are negligible.

4.1.1. Two-dimensional Gaussian bump

Consider the following surface (curve) \mathcal{S} (Figure 3) embedded in a two-dimensional space $d = 2$ ($d' = d - 1 = 1$)

$$\mathcal{S} = \{\mathcal{M}(r) \in \mathbb{R}^2 \mid r \in \mathcal{R}\}, \quad (42)$$

where $\mathcal{R} := (-1.5, 1.5)$ (parameter domain), $\mathcal{M} : r \mapsto (r, f(r))$, and $f : \mathcal{R} \rightarrow (0, a)$, $f : r \mapsto a \exp(-br^2)$ defines the curve, and $a = 1/16$ and $b = 25$. Because f is Gaussian, the surface \mathcal{S} will not be exactly represented by a piecewise polynomial space so the mesh-based parametrization will incur a discretization error. To study the behavior of the mesh-based parametrization under refinement, we define a mesh-based parametrization $\mathcal{M}_{h',q'}$ (Figure 3) and its derivative $M_{h',q'}$ for three grids, $h' = 3/N$ for $N = 12, 120, 1200$ and three polynomial degrees $q = 1, 2, 6$. For this problem, we take $\Pi_{h',q'} : x \mapsto x_1$, which leads to the parameter domain $\mathcal{R}_{h',q'} = \mathcal{R}$.

The mesh-based parametrization show clear convergence as h' decreases or q' increases and, as expected, the error decreases more rapidly with h' for the larger polynomial degrees (Figure 4). At the finest resolution, $N = 1200$ and $q' = 6$, the error in the mesh-based parametrization and its derivative are $\mathcal{O}(10^{-8})$ and $\mathcal{O}(10^{-5})$, respectively, which shows the mesh-based parametrization can be made effectively indistinguishable from a parametrization of the true geometry. We will show in Section 4.2 that implicit shock tracking is still effective when much coarser geometry grids are used.

Remark 11. The mapping $\Pi_{h',q'} : x \mapsto x_1$ used for this problem is obtained from the approach in Appendix A.1 with $\hat{x} = 0$ and $n = (0, 1)$.

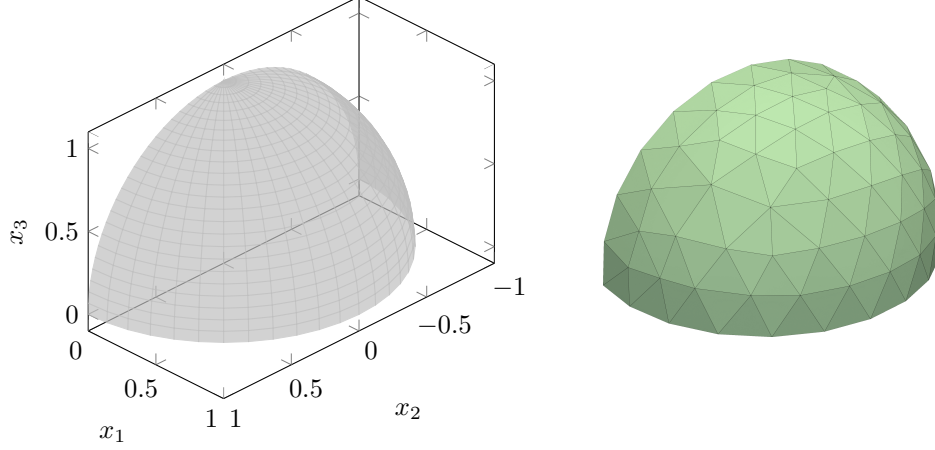


Figure 5: The true surface \mathcal{S} (left) of the quarter sphere and a surrogate surface $\mathcal{S}_{h',q'}$ for $h' \approx 0.15$, $q' = 1$ (right).

4.1.2. Three-dimensional quarter sphere

Consider the following surface \mathcal{S} (Figure 5) embedded in a three-dimensional space $d = 3$ ($d' = d - 1 = 2$)

$$\mathcal{S} = \{\mathcal{M}(r) \in \mathbb{R}^2 \mid r \in \mathcal{R}\}, \quad (43)$$

where $\mathcal{R} = \{r \in \mathbb{R}^2 \mid r_1^2 + r_2^2 \leq 1, r_1 \geq 0\}$ (parameter domain), $\mathcal{M} : r \mapsto (r_1, r_2, f(r_3))$, and $f : \mathcal{R} \rightarrow (0, 1)$, $f : r \mapsto \sqrt{1 - r_1^2 - r_2^2}$ defines the surface. Similar to Section 4.1.1, the surface \mathcal{S} will not be exactly represented by a piecewise polynomial space so the mesh-based parametrization will incur a discretization error. To study the behavior of the mesh-based parametrization under refinement, we define a mesh-based parametrization $\mathcal{M}_{h',q'}$ (Figure 5) and its derivative $M_{h',q'}$ for two grids, $h' = \sqrt{\pi/N}$ for $N = 134,8576$ and two polynomial degrees $q' = 1, 2$. For this problem, we take $\Pi_{h',q'} : x \mapsto (x_1, x_2)$, which leads to $\mathcal{R}_{h',q'}$ being a piecewise polynomial approximation to \mathcal{R} . The error in the mesh-based parametrization (Figure 6) decreases by two orders of magnitude when the polynomial degree is increased from $q' = 1$ to $q' = 2$ or each surface triangle is split into 64 triangles, which demonstrates the effectivity of polynomial refinement over h -refinement. The benefit of polynomial refinement is more pronounced for mesh-based parametrization derivative (Figure 7) as the error decreases by three orders of magnitude when the polynomial degree is increased from $q' = 1$ to $q' = 2$ but just over one order of magnitude by splitting each surface triangle into 64 triangles. Based on this observation we opt for geometry meshes with larger polynomial degrees when integrated into implicit shock tracking (Sections 4.2-4.3) rather than using more elements to improve the geometry resolution.

Remark 12. The mapping $\Pi_{h',q'} : x \mapsto (x_1, x_2)$ used for this problem is obtained from the approach in Appendix A.1 with $\hat{x} = 0$ and $n = (0, 0, 1)$.

4.2. Linear advection: straight-sided shock intersecting curved boundary

Consider steady, linear advection of a scalar quantity $U : \Omega \mapsto \mathbb{R}$ through a domain $\Omega \subset \mathbb{R}^d$, which is a conservation law of the form (24) with $m = 1$ and

$$F : W \mapsto W\beta^T, \quad S : W \mapsto 0, \quad (44)$$

where $\beta : \Omega \mapsto \mathbb{R}^d$ is the flow direction, $U(x)$ is implicitly defined as the solution of (24) with boundary condition $U(x) = U_\infty(x)$ for $x \in \Gamma_{\text{in}}$, $\Gamma_{\text{in}} = \{x \in \partial\Omega \mid \beta(x) \cdot n(x) < 0\}$ is the inflow boundary, and $U_\infty : \partial\Omega \rightarrow \mathbb{R}$ is the boundary condition. In this problem, we consider a two-dimensional domain ($d = 2$) defined as $\Omega := \{x \in \mathbb{R}^2 \mid x_1 \in (-1, 1), x_2 \in (0, f(x_1))\}$, where $f : (-1, 1) \rightarrow \mathbb{R}$ is a polynomial of degree seven, defined as $f : s \mapsto 1 + 0.07(s^2 - 1)(s^5 - 0.1s^4 + 4.9s^3 + 10s^2 - 7.8s - 2.8)$. We also define a constant velocity field $\beta : x \mapsto (0.25, 1)$ with boundary condition $U_\infty : x \mapsto H(x)$, where $H : \mathbb{R} \rightarrow \{0, 1\}$ is the Heaviside function, which leads to a solution with discontinuity along the line $\{(s/4, s) \mid s \in \mathbb{R}_{\geq 0}\}$ with constant solution

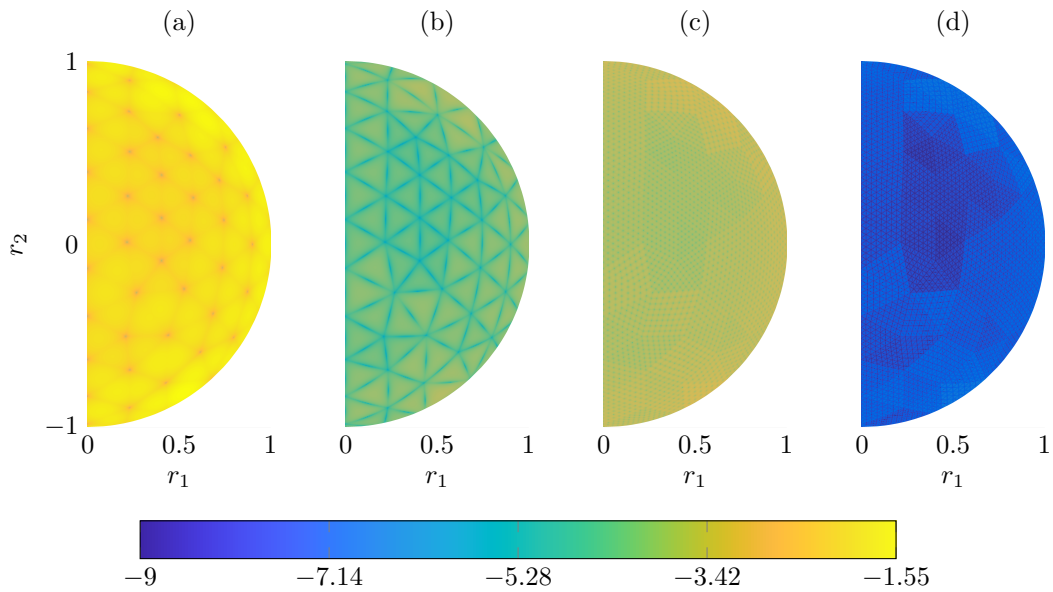


Figure 6: The logarithm (base 10) of the error in the mesh-based parametrization ($\log_{10} E(r)$) for two refinement levels ($N = 134, 8576$) and polynomial degrees ($q' = 1, 2$). Legend: (a) $N = 134$, $q' = 1$, (b) $N = 134$, $q' = 2$, (c) $N = 8576$, $q' = 1$, (d) $N = 8576$, $q' = 2$.

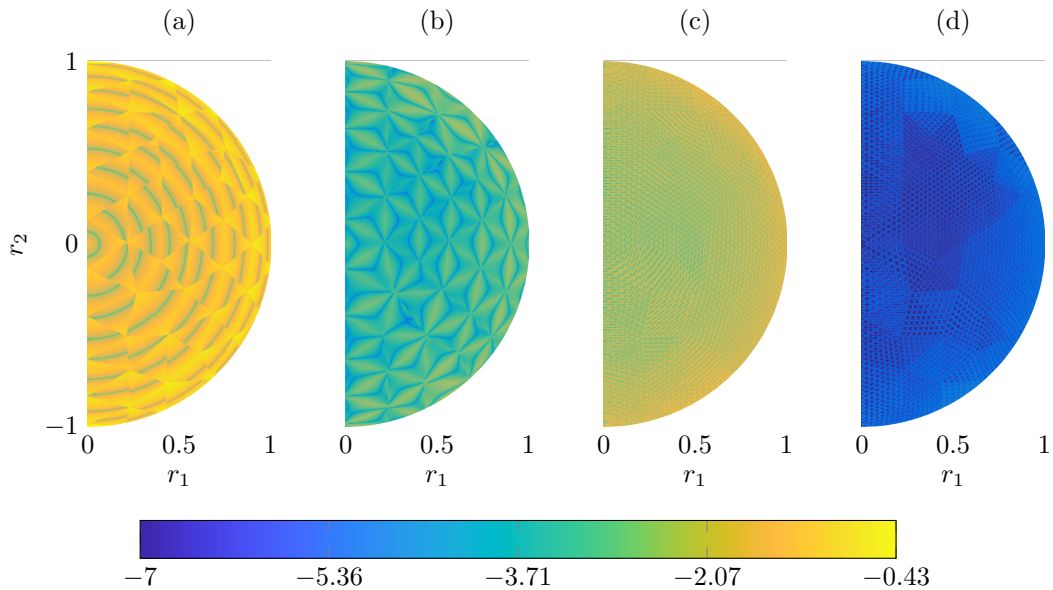


Figure 7: The logarithm (base 10) of the error in the mesh-based parametrization derivative ($\log_{10} E_{\partial}(r)$) for two refinement levels ($N = 134, 8576$) and polynomial degrees ($q' = 1, 2$). Legend: (a) $N = 134$, $q' = 1$, (b) $N = 134$, $q' = 2$, (c) $N = 8576$, $q' = 1$, (d) $N = 8576$, $q' = 2$.

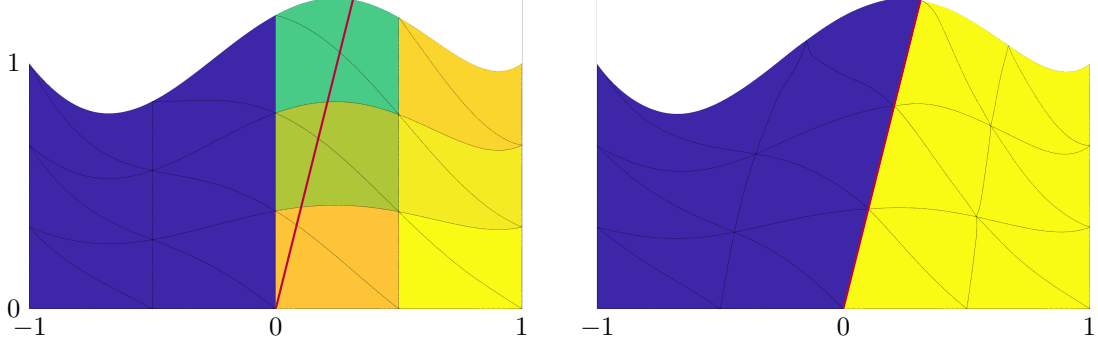


Figure 8: Initial $p = 0$ solution (*left*) and converged HOIST solution (*right*) of the linear advection problem with the true discontinuity surface highlighted (—).

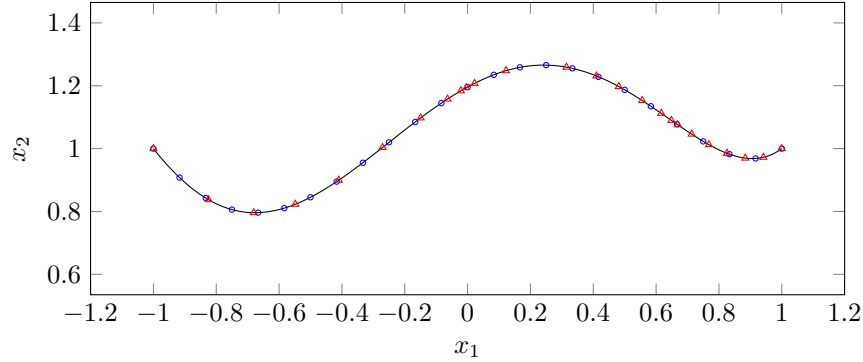


Figure 9: The surrogate surface of the upper boundary for the linear advection problem (—) with the initial (\circ) and final (\triangle) positions of the high-order nodes on this boundary.

on either side. All four boundaries (including the planar ones) and their intersections (in $d = 2$, points at the intersection of two boundaries are fixed) are parametrized using mesh-based parametrization (16) with $h' = \ell_i/4$ and $q' = 6$, where ℓ_i is the length of boundary i . The mesh-based parametrization ϕ is slightly modified to fix the node at $(0, 0)$ to ensure the discontinuous boundary condition is represented correctly, i.e., $\phi_I(\mathbf{y}_I) = \mathbf{X}_I$ where $I \in \{1, \dots, N_x\}$ such that $\mathbf{X}_I = (0, 0)$. The domain is discretized into 24 triangular elements with $q = 6$ domain approximation and $p = 0$ solution approximation. The DG discretization uses the smoothed Riemann numerical flux described in [40, 39].

Starting from a shock-agnostic mesh and a first-order finite volume solution, the HOIST method converges to a mesh with element faces aligned with the discontinuity and an accurate flow solution (Figure 8). Nodes on the top boundary slide perfectly along the top surrogate surface using the mesh-based parametrization ϕ (Figure 9) constructed using the framework in Section 2 (without using the analytical expression of the boundary, only the geometry mesh, $\hat{\Omega}_{h', q'}$). In only $k = 33$ iterations, the residual reaches decreases nearly eight orders of magnitude and the enriched residual decreases four orders of magnitude (Figure 10).

4.3. Inviscid, transonic flow over RAE2822 airfoil

In this section we consider steady fluid flow in an inviscid, compressible fluid through a domain $\Omega \subset \mathbb{R}^d$ governed by the Euler equations of gasdynamics (24) with

$$U = \begin{bmatrix} \rho \\ \rho v \\ \rho E \end{bmatrix}, \quad F : U \mapsto \begin{bmatrix} \rho v v^T \\ \rho v v^T + P I_{d \times d} \\ (\rho E + P) v^T \end{bmatrix}, \quad S : U \mapsto \begin{bmatrix} 0 \\ 0_d \\ 0 \end{bmatrix}. \quad (45)$$

The density $\rho : \Omega \mapsto \mathbb{R}_{>0}$, velocity $v_i : \Omega \mapsto \mathbb{R}$ and the energy $E : \Omega \mapsto \mathbb{R}_{>0}$ are defined implicitly as the solution of (24) and (45). For a calorically perfect fluid, the pressure $P : x \mapsto \mathbb{R}_{>0}$ is related to the energy

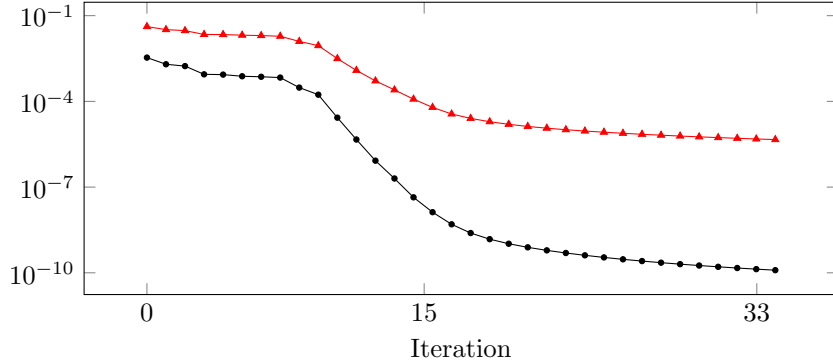


Figure 10: Convergence of the standard (—●—) and enriched (—▲—) DG residual as a function of the HOIST SQP iterations.

by the ideal gas law

$$P = (\gamma - 1) \left(\rho E - \frac{\rho v_i v_i}{2} \right), \quad (46)$$

where $\gamma \in \mathbb{R}_{>0}$ is the ratio of specific heats.

In this problem, we consider transonic flow at Mach number $M = 0.82$ and angle of attack $\alpha = 0.92^\circ$ over the RAE2822 airfoil with chord length $c = 1$ and $\gamma = 1.4$. The left and right boundaries are two chords lengths from the airfoil and the top and bottom boundaries are three chord lengths away. The farfield conditions $\rho_\infty = 1$, $P_\infty = 1/\gamma$ are enforced using Roe’s numerical flux, i.e., solving an approximate Riemann problem between the interior and boundary state. A no-penetration ($v \cdot n = 0$) is enforced on the airfoil surfaces. The conservation law is discretized using DG on a mesh ($\hat{\Omega}_{h,q}$) consisting of 755 quadratic ($q = 2$) triangular elements with quadratic ($p = 2$) flow approximation. We use the Roe flux with Harten-Hyman entropy fix [11]. The boundary-preserving parametrization ϕ is constructed via mesh-based parametrization of the upper and lower surfaces of the airfoil and fixed nodes on the farfield boundaries. Under this parametrization, the nodes on the leading and trailing edge remain fixed because these points represent the intersection of two surfaces (i.e., the upper and lower airfoil) in two dimensions (Section 2.2). The geometry mesh of the airfoil surfaces is extracted from the computational mesh ($h' = h$, $q' = q$).

Starting from a shock-agnostic mesh and first-order finite volume solution, the HOIST method aligns the mesh with both shocks, the strong shock on the upper surface and the weak shock on the lower surface (Figure 11). Even though there is no analytical expression for the RAE2822 surfaces, the nodes slide along the top and bottom surrogate surfaces of the airfoil in such a way that preserves the geometry of the airfoil using mesh-based parametrization (Figure 12). In only $k = 100$ iterations, the residual decreases almost three orders of magnitude and the enriched residual decreases almost two orders of magnitude (Figure 13). This problem demonstrates the ability of the HOIST method to track multiple shocks of different strengths, and the effectivity of mesh-based parametrization in pinning nodes to their original surfaces, even for geometries without analytical expressions (only a geometry mesh of the surfaces and their intersections is required).

4.4. Mesh-based parametrization of the sliced cone flap geometry

We close with a demonstration of mesh-based parametrization for a complex three-dimensional geometry ($d = 3$), the sliced cone flap [26] (Figure 14). This geometry has seven main surfaces: the upper and lower surface of the cone, the slice, the back, and the three surfaces of the flap (the incline and two sides) (Figure 15). We construct a geometry mesh of all six surfaces consisting of 2088 triangular elements of degree $q' = 2$. From these conforming surface meshes, we also extract the geometry meshes of the intersections. We construct the parameter domain, $\mathcal{R}_{h',q'} \subset \mathbb{R}^2$ for the upper cone surface, the slice, and the flap incline using the approach in Appendix A (Figure 16). Then, we define a curve $\mathcal{C} \subset \mathcal{R}_{h',q'}$ (spiral pattern) in the parameter domain of the three surfaces and apply the mesh-based parametrization to each point in \mathcal{C} , which forms a curve that traverses the corresponding surrogate surfaces in physical space (\mathbb{R}^3) (Figure 16). Next, we construct the parameter domain $\mathcal{R}_{h',q'} \subset \mathbb{R}$ and mesh $\hat{\mathcal{R}}_{h',q'}$ of the intersection of the upper cone and slice surfaces (Figure 17). Finally, the mesh-based parametrization of this intersection is used to map five points in $\mathcal{R}_{h',q'}$ to the intersection of these surrogate surfaces in physical space (\mathbb{R}^3) (Figure 17).

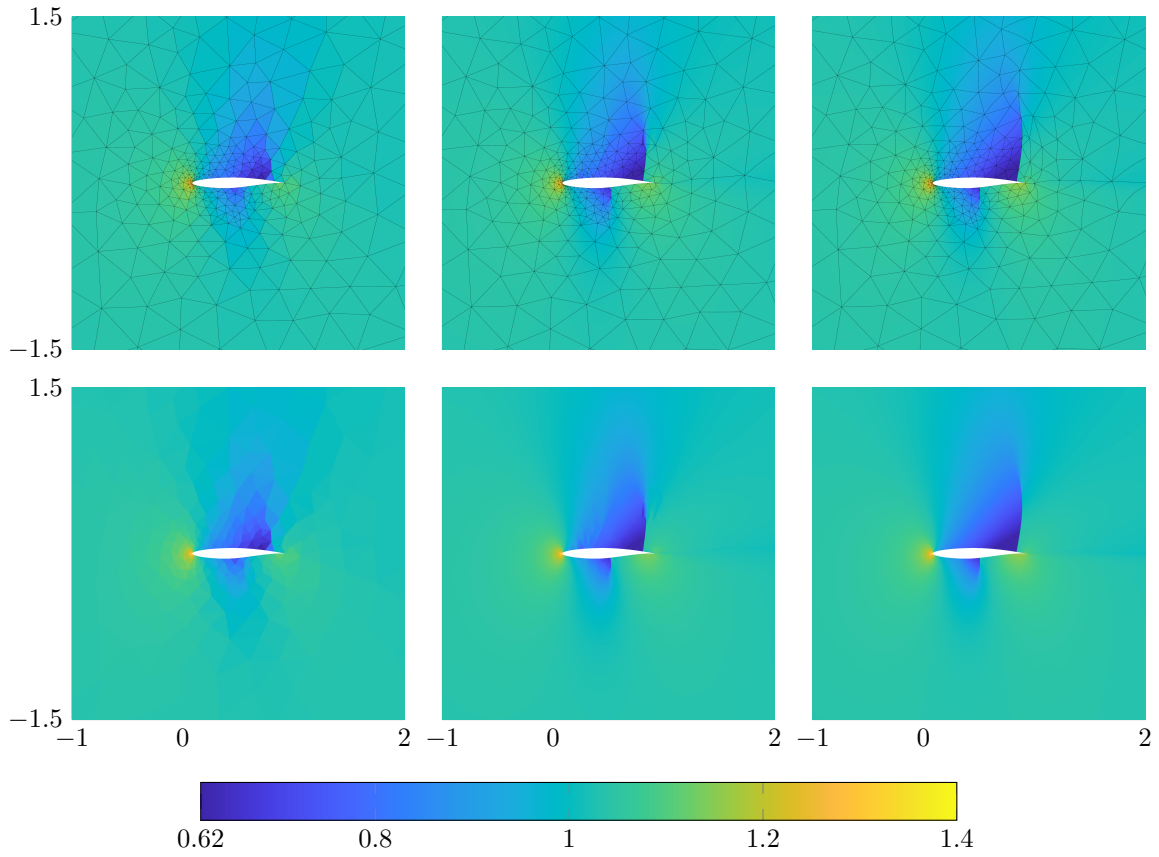


Figure 11: Initial $p = 0$ solution (left), an unconverged SQP iteration ($k = 7$) (middle), and converged HOIST solution (right) of the RAE2822 problem.

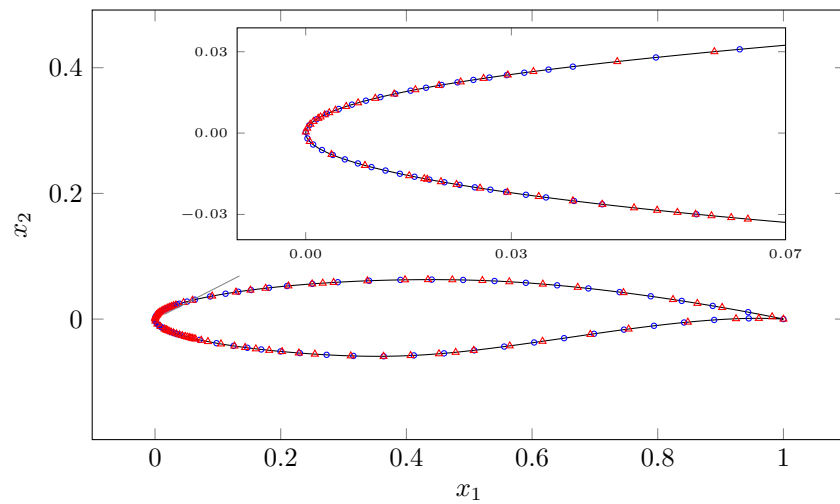


Figure 12: The surrogate surface of the RAE2822 airfoil (—) and the surface nodes of the computational mesh in their initial (◉) and final (◄) positions after $k = 100$ HOIST iterations.

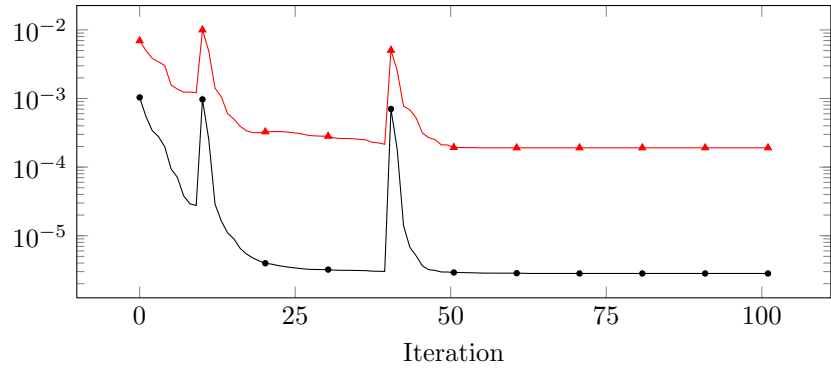


Figure 13: Convergence of the standard (—●—) and enriched (—▲—) DG residual as a function of the HOIST SQP iterations.

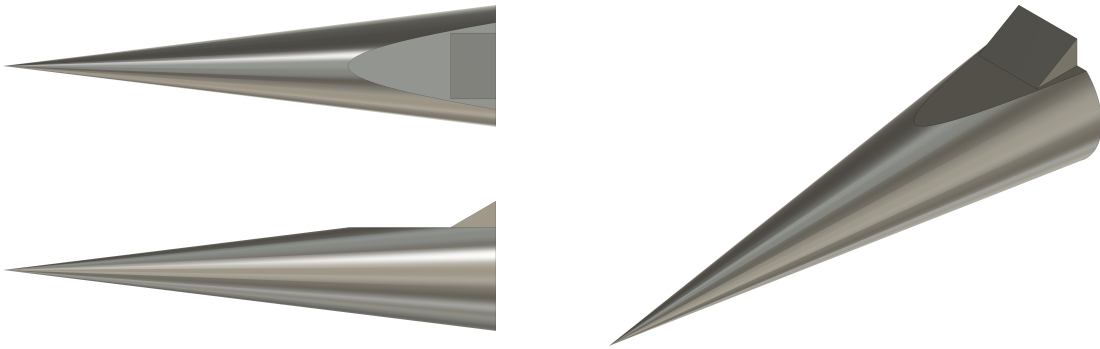


Figure 14: Sliced cone flap geometry.

This example demonstrates that mesh-based parametrization can be used to parametrize the surfaces and surface intersections of complex geometries. Because it only requires a conforming mesh of all surfaces, it is an attractive approach to define the boundary-preserving mappings ϕ for implicit shock tracking. The fact that each surface and surface intersection are parametrized separately means that nodes will always remain on their original boundaries. This simplifies the assignment of boundary conditions to mesh faces and avoids oscillations that would arise if a face straddles two surfaces with a non-smooth transition between them (such as between the cone and slice surfaces).

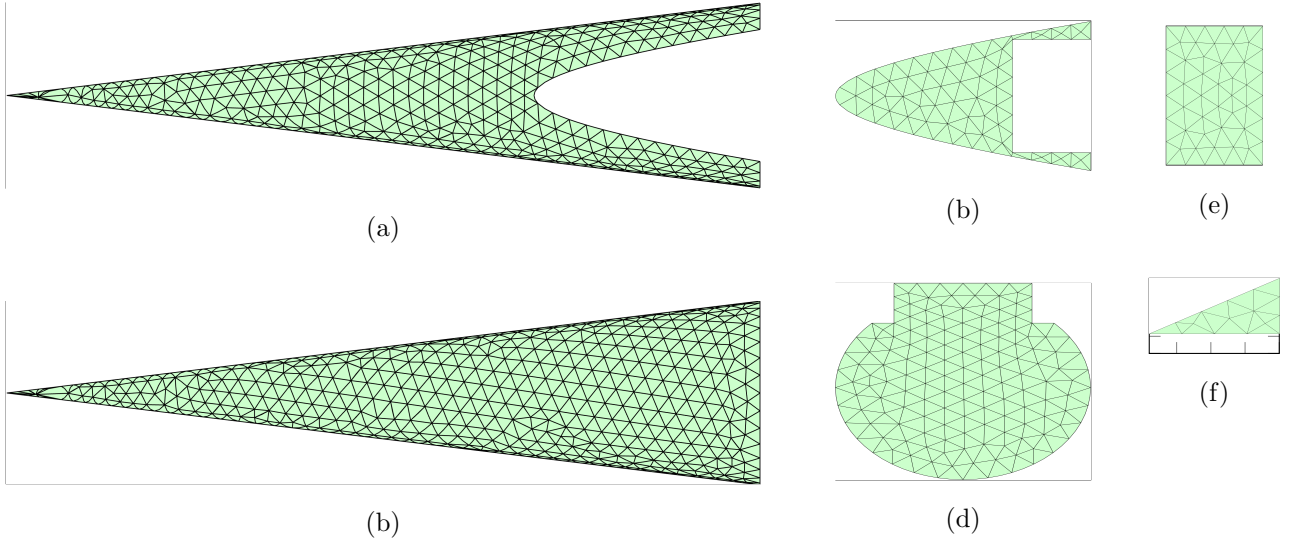


Figure 15: The seven surfaces of the sliced cone flap geometry: (a) upper cone surface, (b) lower cone surface, (c) slice, (d) back, (e) flap incline, and (f) flap side.

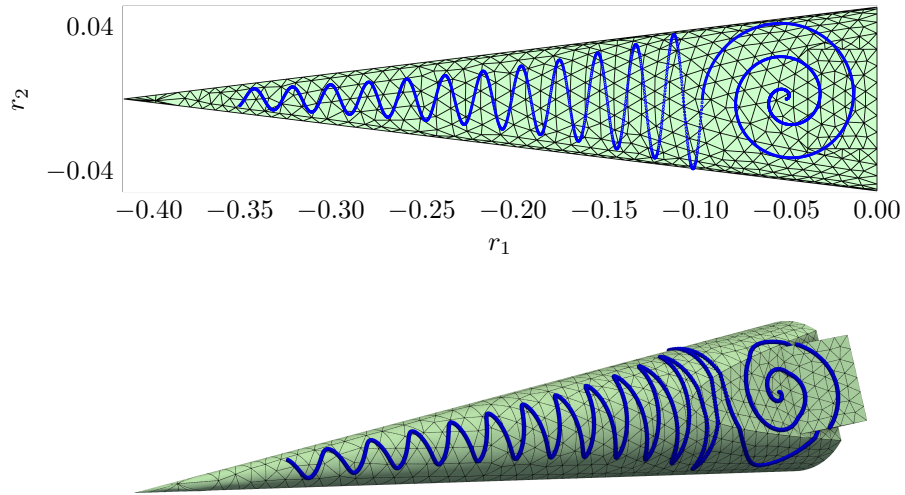


Figure 16: The parameter domain $\mathcal{R}_{h',q'}$ and mesh $\hat{\mathcal{R}}_{h',q'}$ of the upper cone, slice, and flap incline surfaces (*top*) and the sliced cone flap geometry in physical space (*bottom*). A curve (blue) generated in the parameter domain is guaranteed to lie on the surrogate surfaces when mapped with the mesh-based parametrization.

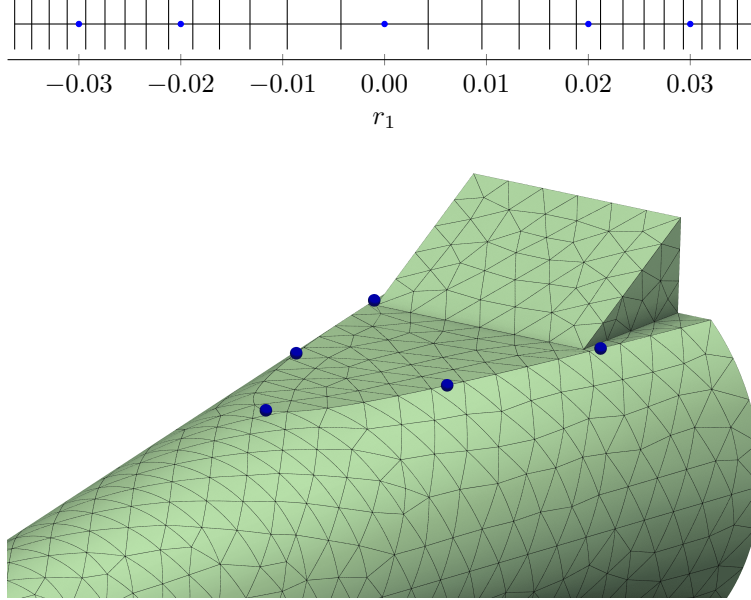


Figure 17: The parameter domain $\mathcal{R}_{h',q'}$ and mesh $\hat{\mathcal{R}}_{h',q'}$ of the intersection of the upper cone and slice surfaces (*top*) and the sliced cone flap geometry in physical space (*bottom*). Nodes (blue) maps from the one-dimensional parameter domain to the intersection of the upper cone and slice surfaces in physical space.

5. Conclusion

A mesh-based parametrization is a mapping from generalized coordinates in the intrinsic dimension of a geometric object to a high-order approximation of the object itself in the embedding space, constructed directly from a high-order mesh of the object, i.e., an analytical expression or CAD representation of the object is not used. We rigorously formulate mesh-based parametrizations of an arbitrary d' -dimensional object embedded in a d -dimensional space using standard tools from high-order finite elements (Section 2.1). Then, we detail an approach to parametrize the nodal coordinates of a computational mesh such that any node is guaranteed to remain on its original boundaries by parametrizing each boundary and all boundary intersections using mesh-based parametrization (Section 2.2). Ensuring nodes remain on their original boundaries guarantees a mesh face will not straddle multiple boundaries, which would make assigning boundary conditions to such a face difficult and would lead to poor geometry representation for non-smooth transitions between boundaries. These boundary-preserving, mesh-based parametrizations are embedded in an implicit shock tracking framework to allow nodes to freely slide along their original boundaries in the process of aligning element faces with non-smooth flow features. It is particularly important to allow boundary nodes to slide for problems where shocks approach or intersect boundaries (e.g., transonic flows, shock-boundary layer interactions) because fixing them would either prohibit shock tracking or highly distort the mesh. As such, the proposed boundary-preserving, mesh-based parametrizations extend shock tracking capabilities to a new class of problems. Because mesh-based parametrizations are defined elementwise, their efficient implementation relies on a fast, reliable method to locate the element(s) of the parameter domain mesh $\hat{\mathcal{R}}_{h',q'}$ in which an arbitrary point $r \in \mathcal{R}_{h',q'}$ lies. We introduce an algorithm, specialized for high-order meshes, to efficiently search the elements of a mesh to locate such a point (Section 2.3).

Two concrete examples of mesh-based parametrizations are provided for analytical geometries, a Gaussian profile ($d = 2$) and a quarter sphere ($d = 3$), to demonstrate the abstract formalism in Section 2.1 and show the surrogate objects accurately approximate the true geometry when sufficiently refined grids (e.g., small h' or large q') are used. Two examples demonstrate boundary-preserving, mesh-based parametrizations cleanly integrate into the implicit shock tracking and do not restrict or impede convergence. Finally, we demonstrate the generality of mesh-based parametrizations using a complex geometry, the sliced cone flap [26]. Future research should investigate the benefits of implicit shock tracking for shock-dominated flows over increasingly complex and relevant vehicles.

Acknowledgments

This work is supported by AFOSR award numbers FA9550-20-1-0236, FA9550-22-1-0002, FA9550-22-1-0004, ONR award number N00014-22-1-2299, and NSF award number CBET-2338843. The content of this publication does not necessarily reflect the position or policy of any of these supporters, and no official endorsement should be inferred.

Appendix A. Restriction of embedded objects to their intrinsic dimension via projection

In this section we detail simple approaches to define the mapping $\Pi_{h',q'}$, and therefore the parameter space $\mathcal{R}_{h',q'}$, by projecting a surface onto a predefined hyperplane (Appendix A.1) and projecting a curve onto a predefined line (Appendix A.2).

Appendix A.1. Projection of surface onto hyperplane

Suppose \mathcal{S} is a surface, i.e., $d' = d - 1$ and define a hyperplane with unit normal $n \in \mathbb{R}^d$, $\|n\| = 1$, that passes through \hat{x} , i.e., $\Phi = \{x \in \mathbb{R}^d \mid (x - \hat{x}) \cdot n = 0\}$. The orthogonal projection of any point $x \in \mathcal{S}_{h',q'}$ onto Φ is the solution of $\arg \min_{r \in \mathbb{R}^{d-1}} \|\hat{x} + Ar - x\|$, where $A \in \mathbb{R}^{d \times (d-1)}$ is a matrix whose rows are the vectors of the nullspace of n , i.e., $A = \text{null}(n)^T$, which means $A \cdot n = 0$. From the analytical solution of this linear least squares problem, we define the projection-based restriction operator $\Pi_{h',q'}$ as

$$\Pi_{h',q'} : x \mapsto (A^T A)^{-1} (A^T (x - \hat{x})). \quad (\text{A.1})$$

While simple, this approach has several drawbacks: the need to define the hyperplane (\hat{x}, n) and, even for an optimal choice of hyperplane, the mapping $\Pi_{h',q'}$ will lose injectivity for non-closed surfaces or surfaces with excessive curvature. Because the framework proposed in this manuscript handles surfaces and arbitrary intersections of surfaces, a closed surface or surface with excessive curvature can be subdivided into smaller open surfaces with less curvature at the expense of additional surfaces and intersections that must be parametrized. As such, even this simple restriction operator works robustly for a wide class of surfaces.

Appendix A.2. Projection of curve onto line

Suppose \mathcal{S} is a curve, i.e., $d' = 1$ and define a line with unit tangent $v \in \mathbb{R}^d$, $\|v\| = 1$, that passes through \hat{x} , i.e., $\Psi = \{x \in \mathbb{R}^d \mid x = \hat{x} + \alpha v, \alpha \in \mathbb{R}\}$. The projection of any point $x \in \mathcal{S}_{h',q'}$ onto Ψ is the solution of $\arg \min_{\alpha \in \mathbb{R}} \|\hat{x} + \alpha v - x\|$. From the analytical solution of this linear least squares problem, we define the projection-based restriction operator $\Pi_{h',q'}$ as

$$\Pi_{h',q'} : x \mapsto v \cdot (x - \hat{x}). \quad (\text{A.2})$$

Similar to Appendix A.1, $\Pi_{h',q'}$ may not be injective for closed curves or curves with high curvature, but this can be circumvented by further subdividing surfaces until their intersections have been sufficiently refined that $\Pi_{h',q'}$ is injective for all subdivided curves.

References

- [1] Jorge-Luis Barrera, Tzanio Kolev, Ketan Mittal, and Vladimir Tomov. High-order mesh morphing for boundary and interface fitting to implicit geometries. *Computer-Aided Design*, 158:103499, 2023.
- [2] Garrett E. Barter and David L. Darmofal. Shock capturing with PDE-based artificial viscosity for DGFEM: Part I. Formulation. *Journal of Computational Physics*, 229(5):1810–1827, March 2010.
- [3] J. B. Bell, G. R. Shubin, and J. M. Solomon. Fully implicit shock tracking. *Journal of Computational Physics*, 48(2):223–245, 1982.

- [4] Kristoffer Carlsson, Daniel Karrasch, Nicholas Bauer, Okon Samuel, Tony Kelman, Josh Christie, Pablo San-Jose, Martijn Visser, Júlio Hoffmann, Elias Carvalho, Ed Schmerling, Tamas Nagy, Shushman Choudhury, Ilya Orson, Gustavo Goretkin, Fredrik Ekre, Elliot Saba, David Muhr, Claire Foster, Carlo Lucibello, Benoit Pasquier, Anthony Blaom, and Andy Ferris. KristofferC/NearestNeighbors.jl: v0.4.21, November 2024.
- [5] Bernardo Cockburn and Chi-Wang Shu. Runge–Kutta discontinuous Galerkin methods for convection-dominated problems. *Journal of Scientific Computing*, 16(3):173–261, September 2001.
- [6] Andrew Corrigan, Andrew Kercher, and David Kessler. A moving discontinuous Galerkin finite element method for flows with interfaces. *International Journal for Numerical Methods in Fluids*, 89(9):362–406, 2019.
- [7] Andrew Corrigan, Andrew Kercher, and David Kessler. The moving discontinuous Galerkin method with interface condition enforcement for unsteady three-dimensional flows. In *AIAA Scitech 2019 Forum*, AIAA-2019-0642.
- [8] Andrew Corrigan, Andrew Kercher, David Kessler, and Devon Wood-Thomas. Convergence of the moving discontinuous Galerkin method with interface condition enforcement in the presence of an attached curved shock. In *AIAA Aviation 2019 Forum*, AIAA-2019-3207.
- [9] C. Geuzaine, A. Johnen, J. Lambrechts, J. F. Remacle, and T. Toulorge. The generation of valid curvilinear meshes. In Norbert Kroll, Charles Hirsch, Francesco Bassi, Craig Johnston, and Koen Hillewaert, editors, *IDIHOM: Industrialization of High-Order Methods - A Top-Down Approach: Results of a Collaborative Research Project Funded by the European Union, 2010 - 2014*, pages 15–39. Springer International Publishing, 2015.
- [10] James Glimm, Xiaolin Li, Yingjie Liu, Zhiliang Xu, and Ning Zhao. Conservative Front Tracking with Improved Accuracy. *SIAM Journal on Numerical Analysis*, 41(5):1926–1947, January 2003. Publisher: Society for Industrial and Applied Mathematics.
- [11] A. Harten and J. M. Hyman. Self adjusting grid methods for one-dimensional hyperbolic conservation laws. *Journal of Computational Physics*, 50(2):235–269, 1983.
- [12] Ami Harten, Bjorn Engquist, Stanley Osher, and Sukumar R Chakravarthy. Uniformly high order accurate essentially non-oscillatory schemes, III. *Journal of Computational Physics*, 71(2):231–303, August 1987.
- [13] Jan S. Hesthaven and Tim Warburton. *Nodal Discontinuous Galerkin Methods: Algorithms, Analysis, and Applications*. Texts in Applied Mathematics. Springer-Verlag, New York, 2008.
- [14] Tianci Huang and Matthew J. Zahr. A robust, high-order implicit shock tracking method for simulation of complex, high-speed flows. *Journal of Computational Physics*, 454:110981, 2022.
- [15] Guang-Shan Jiang and Chi-Wang Shu. Efficient implementation of weighted ENO schemes. *Journal of Computational Physics*, 126(1):202–228, June 1996.
- [16] Andrew D. Kercher and Andrew Corrigan. A least-squares formulation of the moving discontinuous Galerkin finite element method with interface condition enforcement. *Computers & Mathematics with Applications*, 2020.
- [17] Andrew D. Kercher, Andrew Corrigan, and David A. Kessler. The moving discontinuous Galerkin finite element method with interface condition enforcement for compressible viscous flows. *International Journal for Numerical Methods in Fluids*, 2020.
- [18] Patrick Knupp, Tzanio Kolev, Ketan Mittal, and Vladimir Z Tomov. Adaptive surface fitting and tangential relaxation for high-order mesh optimization. <https://arxiv.org/abs/2105.12165>, 2021.
- [19] Patrick M. Knupp. Algebraic mesh quality metrics. *SIAM Journal on Scientific Computing*, 23(1):193–218, January 2001.

- [20] Roland Krause and Ernst Rank. A fast algorithm for point-location in a finite element mesh. *Computing*, 57:49–62, 1996.
- [21] Xu-Dong Liu, Stanley Osher, and Tony Chan. Weighted essentially non-oscillatory schemes. *Journal of Computational Physics*, 115(1):200–212, November 1994.
- [22] Ketan Mittal, Veselin A Dobrev, Patrick Knupp, Tzanio Kolev, Franck Ledoux, Claire Roche, and Vladimir Z Tomov. Mixed-order meshes through rp-adaptivity for surface fitting to implicit geometries. In *Proceedings of the 2024 International Meshing Roundtable (IMR)*, pages 118–131. SIAM, 2024.
- [23] G. Moretti. Thirty-six years of shock fitting. *Computers & Fluids*, 31(4-7):719–723, 2002.
- [24] Charles J. Naudet and Matthew J. Zahr. A space-time high-order implicit shock tracking method for shock-dominated unsteady flows. *Journal of Computational Physics*, 501:112792, 2024.
- [25] Azad Noorani, Adam Peplinski, and Philipp Schlatter. Informal introduction to program structure of spectral interpolation in nek5000. Technical report, Tech. Rep., KTH Royal Institute of Technology, 2015.
- [26] William L. Oberkampf and Daniel P. Aeschliman. Joint computational/experimental aerodynamics research on a hypersonic vehicle. i - experimental results. *AIAA Journal*, 30(8):2000–2009, 1992.
- [27] P-O Persson, Javier Bonet, and Jaime Peraire. Discontinuous Galerkin solution of the Navier–Stokes equations on deformable domains. *Computer Methods in Applied Mechanics and Engineering*, 198(17-20):1585–1595, 2009.
- [28] Per-Olof Persson and Jaime Peraire. Sub-cell shock capturing for discontinuous Galerkin methods. In *44th AIAA Aerospace Sciences Meeting and Exhibit*. AIAA Paper 2006-112, 2006.
- [29] Xevi Roca, Abel Gargallo-Peiró, and Josep Sarrate. Defining quality measures for high-order planar triangles and curved mesh generation. In William Roshan Quadros, editor, *Proceedings of the 20th International Meshing Roundtable*, pages 365–383, Berlin, Heidelberg, 2012. Springer.
- [30] Philip L. Roe. Approximate Riemann solvers, parameter vectors, and difference schemes. *Journal of Computational Physics*, 43(2):357–372, 1981.
- [31] M.D. Salas. *A shock-fitting primer*. CRC Press, 2009.
- [32] G. R. Shubin, A. B. Stephens, and H. M. Glaz. Steady shock tracking and Newton’s method applied to one-dimensional duct flow. *Journal of Computational Physics*, 39(2):364–374, 1981.
- [33] G. R. Shubin, A. B. Stephens, H. M. Glaz, A. B. Wardlaw, and L. B. Hackerman. Steady shock tracking, Newton’s method, and the supersonic blunt body problem. *SIAM Journal on Scientific and Statistical Computing*, 3(2):127–144, 1982.
- [34] Thomas Toulorge, Jonathan Lambrechts, and Jean-Fran çois Remacle. Optimizing the geometrical accuracy of curvilinear meshes. *Journal of Computational Physics*, 310:361–380, 2016.
- [35] Bram Van Leer. Towards the ultimate conservative difference scheme. V. A second-order sequel to Godunov’s method. *Journal of Computational Physics*, 32(1):101–136, 1979.
- [36] J. Van Rosendale. Floating shock fitting via lagrangian adaptive meshes. Technical Report ICASE Report No. 94-89, Institute for Computer Applications in Science and Engineering, 1994.
- [37] Z. J. Wang, Krzysztof Fidkowski, Rémi Abgrall, Francesco Bassi, Doru Caraeni, Andrew Cary, Herman Deconinck, Ralf Hartmann, Koen Hillewaert, H. T. Huynh, Norbert Kroll, Georg May, Per-Olof Persson, Bram van Leer, and Miguel Visbal. High-order CFD methods: current status and perspective. *International Journal for Numerical Methods in Fluids*, 72(8):811–845, 2013.
- [38] Zhong Q Xie, Ruben Sevilla, Oubay Hassan, and Kenneth Morgan. The generation of arbitrary order curved meshes for 3d finite element analysis. *Computational Mechanics*, 51:361–374, 06 2012.

- [39] Matthew J. Zahr and Per-Olof Persson. An optimization-based approach for high-order accurate discretization of conservation laws with discontinuous solutions. *Journal of Computational Physics*, 365:105–134, 2018.
- [40] Matthew J. Zahr and Joseph M. Powers. High-order resolution of multidimensional compressible reactive flow using implicit shock tracking. *AIAA Journal*, 59(1):150–164, December 2020.
- [41] Matthew J. Zahr, Andrew Shi, and Per-Olof Persson. Implicit shock tracking using an optimization-based high-order discontinuous Galerkin method. *Journal of Computational Physics*, 410:109385, June 2020.